Research paper

Study of the Ground Level Enhancements effect on atmospheric electric properties and mineral dust particle charging

Sotirios A. Mallios [a,*], Athanasios Papaioannou [a], Konstantin Herbst [b], Georgios Papangelis [a], George Hloupis [c]

[a] *Institute for Astronomy, Astrophysics, Space Applications and Remote Sensing (IAASARS), National Observatory of Athens, I. Metaxa & Vas. Pavlou St., 15236, Penteli, Greece*
[b] *Institut für Experimentelle und Angewandte Physik, Christan-Albrechts-Universität zu Kiel, Leibnizstr. 11, D-24118, Kiel, Germany*
[c] *Department of Surveying and GeoInformatics Engineering, Faculty of Engineering, University of West Attica, Ag. Spyridonos Street, 12243, Aigaleo, Greece*

ARTICLE INFO

ABSTRACT

The effect of Ground Level Enhancements (GLEs) on the atmospheric and dust particles electrical properties is studied. It has been found that in the case of fair weather conditions, GLE events enhance the atmospheric electrical conductivity, reduce the columnar resistance, and modify the fair weather electric field, air–earth conduction current, and possibly the Ionospheric Potential (IP) in a way that depends on the geomagnetic cut-off rigidity of the location and the altitude. If a dust particle layer is present, GLE events tend to cancel its electrical effects in the ambient atmosphere. This means that the enhancement of the electric field and the reduction of atmospheric electrical conductivity, caused by the ion attachment to dust particles, not only tend to return to their ambient fair weather values, but they can be further modified as if the dust layer was not present. Finally, in terms of dust particles' electrical properties, GLE events tend to modify the ion attachment mechanism, and in principle, the particle net charge, and the electric field "sensed" by them, increase. Nevertheless, since the electrical force magnitude is up to six orders of magnitude less than gravity, the increase of the particles' electrical properties is not sufficient to modify the particle settling dynamics and settling velocities.

1. Introduction

The Global Electric Circuit (GEC) is a manifestation of the electric current pathway in Earth's atmosphere. It is established between the Earth's surface, which is a good conductor of electricity, and the ionosphere, a weakly ionized plasma at ∼80 km altitude (e.g. Rycroft et al., 2008). In the absence of any source, the GEC behaves as a leaky spherical capacitor, with the ground being the one plate and the ionosphere the other, which discharges through the weakly conducting atmosphere creating a conduction current that flows from the ionosphere to the ground, that assuming fair-weather conditions globally is about 1kA integrated over the entire Earth's surface (e.g. Bering et al., 1998).

There are three quasi-DC sources of electromotive force that drive the GEC: thunderstorms, a dynamo interaction between the solar wind and the magnetosphere, and the dynamo effect of atmospheric tides in the thermosphere (Bering et al., 1998, and references therein). Thunderstorms are believed to be the most powerful among these three

sources, by a factor of three (Roble, 1991). Thunderstorms and electrified clouds generate electric currents that flow upwards to the ionosphere through the conducting atmosphere, where part of it spreads horizontally in the equalization layer (the region above about 70 km that has almost constant potential) and the rest flows along the magnetic field lines to the conjugate hemisphere, where it produces a downward-directed fair-weather electric field (Tzur and Roble, 1985). The dynamo in the ionosphere is produced by tides generated in situ and tides propagating upward from the lower atmosphere, generating horizontal potential differences of 5–15 kV with the current flow of ∼10^5 A within the ionosphere (Siingh et al., 2007). Finally, the magnetospheric dynamo is driven by the interaction of the solar wind with the Earth's geomagnetic field and generates a horizontal dawn-to-dusk potential drop of ∼40–100 kV across the magnetic conjugate polar cap (Siingh et al., 2007). An overview of the GEC generators, along with details on their physical mechanisms, can be found in works by Roble (1991), Siingh et al. (2007), and Tinsley (2008).

---

* Corresponding author.
  E-mail address: smallios@noa.gr (S.A. Mallios).

The electrical conductivity of Earth's atmosphere is attributed to the presence of ions. Three mechanisms create the atmospheric ions (Tinsley and Zhou, 2006, and references therein): (1) natural radioactivity originating in the ground, including direct α, β, and γ radiation from the surface layers and dust aerosol, and radiation from radioactive gases (principally 222 Rn but also 220 Rn) and their daughter products. (2) Cosmic rays (CRs) of Galactic and Solar origin, with the second being an occasional source (e.g. Mironova et al., 2015). (3) Relativistic electrons (of a few MeV) precipitated from the radiation belts and peaking at subauroral latitudes, and the Solar Energetic Particle (SEP) events (mainly protons) in the polar and subpolar regions (Mishev, 2013).

Therefore, the investigation of ionization processes within the Earth's atmosphere is vital for understanding and quantifying the coupling of the Sun–Earth system. In particular, CRs influence, through ionization, electrical parameters of planetary atmospheres and the atmospheric chemistry, i.e., the ozone depletion in the stratosphere (see Velinov et al., 2013, and references therein). CRs mainly consist of protons of extraterrestrial origin characterized by high and extremely high energies (see, e.g., Dorman, 2004). These primary particles arrive at Earth, pass through our planet's magnetic field, and impinge at the Earth's atmosphere. CRs with energies ≥ 1 GeV/nuc further interact with the atmospheric constituents by generating secondary particles. Such interactions trigger the nuclear-electromagnetic-muon cascade (Mishev and Velinov, 2014) which directly results in the ionization of the ambient air. In particular, this is achieved as follows: upon the unfolding of the cascade, only a small fraction of the initial energy of the primary particle reaches the ground in the form of high-energy secondary particles. The largest part of the energy of the incoming primary particle is released in the atmosphere by ionization and excitation of the air molecules. Thereby, CRs are an essential source of ionization within the Earth's atmosphere (Bazilevskaya et al., 2008). Based on their sources and achieved energies, there are mainly two populations of CRs that affect the atmosphere: (a) Galactic Cosmic Rays (GCRs) and (b) SEPs (Dorman, 2004). GCRs are modulated by the solar activity and follow an 11 year cycle in an inverse phase with respect to our host's star activity as measured, e.g., by the number of sunspots. That means that the maximum of the GCRs flux is obtained when the lowest of the solar activity (i.e., solar minimum) is marked and vice versa (Gieseler et al., 2017). However, GCRs are ever-present and have a significant imprint on Earth's ionization, especially in the stratosphere and the troposphere (Usoskin et al., 2009). High-energy SEPs enter the atmosphere and lead to significant enhancements above the GCR background, termed as Ground Level Enhancement (GLE) events (Mishev et al., 2014; Papaioannou et al., 2014). These are accelerated during violent phenomena on the Sun, such as solar flares and coronal mass ejections (CMEs) (see, e.g., Papaioannou et al., 2016) and constitute the high energy tail of SEPs (Gopalswamy et al., 2013; Poluianov et al., 2017). As a result, GLEs are particles that appear sporadically, being mostly favored in periods of intense solar activity with their rate being ~1 such event per year. All GLEs are accompanied by a lower-energy SEP part (Souvatzoglou et al., 2014), but not all SEP events result in GLEs. The effect of SEPs in the atmosphere depends on their energy directly related to their penetrating ability. Therefore, GLEs (with energies ≥ 433 MeV) have a direct effect down to the ground level (0 km), whereas lower energy SEPs (e.g., 10 MeV) impact the atmosphere only down to ~65 km above ground level (see, e.g., Fig. 9 in Banjac, Herbst, and Heber, 2019).

The electrical conductivity, and consequently the GEC electric current and electric field, are influenced by clouds. Clouds in the fair weather return path of the GEC reduce conductivity because of the ion attachment to cloud water droplets, effectively leading to a loss of ions (Zhou and Tinsley, 2007, 2012; Baumgaertner et al., 2014; Harrison et al., 2020). Similar effects on the atmospheric conductivity are attributed to aerosols (e.g. Yair and Levin, 1989, and references therein).

Amongst the aerosols affecting the atmospheric electrical content, mineral dust represents one of the most significant contributors, along with volcanic ash (Harrison et al., 2010), due to its mineralogical composition that results in different electrical properties of the dust particles (Kamra, 1972) and its abundance in terms of dry mass (Tegen et al., 1997). Mineral dust, and in general aerosols, are also influenced by the GEC. The ion attachment is one of the charging mechanisms of dust particles (Mallios et al., 2021b). The electrical force acting upon the charged particles in the presence of modified atmospheric electric field has been proposed as a mechanism that could facilitate long-range transport of large giant particles (Nicoll et al., 2010; Renard et al., 2018; Toth III et al., 2020), as they travel from the Sahara desert across the Atlantic ocean to Barbados (Weinzierl et al., 2017; van der Does et al., 2018), to South America (e.g. Barkley et al., 2021), or towards the Balkans, central Europe, even to Iceland (e.g. Đorđević et al., 2019; Varga et al., 2021). Additionally, it can modify the orientation of dust particles, influencing their transport and dynamics (Ulanowski et al., 2007; Mallios et al., 2021a).

Therefore, it is clear that can be a strong connection between solar phenomena with the electrical properties of the Earth's atmosphere and on the dynamics of atmospheric particles. Several works in the past literature investigate this coupling.

Cobb (1967) provided evidence of a direct solar influence on some of the electric elements recorded at the Mauna Loa Observatory, Hawaii. An analysis of the data showed that following a solar flare eruption, both the air–earth conduction current and the electric field, measured during fair weather, usually exceeded their established typical values. The mean value of the air–earth conduction current and the electric field on "disturbed" solar days exceeded that of the "quiet" solar days by about 10%. During the month of July 1961, a period of spectacular solar activity, the highest sustained values of the year for the air–earth current and the electric field were recorded with the normal 24 hr. Values being exceeded by as much as 35%, and for one 6 hr. period following a multiple flare burst, by 75%.

Reiter (1969) recorded the fair weather electric field and the fair weather air–earth current at high-elevation mountain stations. Both electrical quantities increased significantly from the day of the appearance of a solar flare (or a maximum incidence of flares) till the fourth day after the event. Peak electric field magnitude and air–earth current exceed the "normal levels" measured during quiet-sun conditions by ~50% in terms of averages.

Markson (1978) proposed a physical mechanism to explain the solar influence on the atmospheric electrical properties, according to which the enhancement of atmospheric ionization results in the increase of the electrical conductivity above thunderstorms, leading to amplification of the thunderstorm output current, and consequently on the Ionospheric Potential (IP) and the fair weather current and electric field magnitude. In this analysis, thunderstorms were assumed to be voltage sources of the GEC. These findings were later discussed by Willett (1979), who showed that the effect of conductivity perturbations in the upper atmosphere strongly depends on the chosen description of GEC generators, and in the case of the thunderstorms being current sources, this effect is not significant.

Holzworth and Mozer (1979) presented experimental evidence for the effect of solar flares on stratospheric electrical phenomena by comparing atmospheric electric field variations with fluxes of solar protons that bombarded the atmosphere during the August 1972 solar flares. The observed order of magnitude variations of the vertical electric field at 30 km altitude in anti-correlation with the intensity of solar protons were quantitatively interpreted in terms of atmospheric conductivity enhancement produced by solar proton ionization of the air.

Hays and Roble (1979) developed a quasi-static 3D spherical model to examine the electrical coupling between the Earth's upper and lower atmospheric regions. Among others, the perturbation of the calculated electric potential and current distributions was studied due to an increase in CRs during a solar flare, and the subsequent Forbush

decrease. It was derived that the calculated global electrical resistance decreased during the solar flare (as the CR intensity above the earth's surface increases) and then increased during the Forbush decrease. The calculated IP decreased during the CR increase but increased during the subsequent Forbush decrease. The total current decreased, then increased during the same sequence. The ground electric fields at both the equator and the pole were also modulated, decreasing first and later increasing. It was concluded that the conductivity changes due to a solar flare are capable of altering the electrical circuit on a global scale.

Sartor (1980) observed an enhanced effect on the electrification of extensive high-level clouds of the air–earth current associated with solar flares. Following a solar eruption, the Mauna Loa, Hawaii, observations reported increased electric fields of 1.35–1.75 times normal, which could be expected to persist over a lifetime comparable to the lifetime of clouds or the atmospheric conditions responsible for the clouds. The disturbed conditions outside the cloud are enhanced inside and are large enough in precipitating clouds to initiate further charging by the polarization–induction mechanism (through particle collisions).

Markson (1981) derived positive correlations between cosmic radiation and IP, indicating that the electrification of the atmosphere is modulated by changes in ionizing radiation. A 10% change in ground-level cosmic radiation is associated with a 10%–20% variation in IP. No correlation was found due to magnetospheric–ionospheric coupling, suggesting that the ionizing radiation must affect atmospheric electrification through regulation of the thunderstorms' electrical current output, which maintains the fair weather electric field, otherwise increased conductivity in the fair weather part of the atmosphere would lower IP.

Holzworth et al. (1987) presented an analysis of the electric field, conductivity, and ionization rate data, collected on two balloon payloads at 26 km altitude, in the southern hemisphere stratosphere, during the solar flare of 16 February 1984. Both polarities of the conductivity were enhanced by a factor of two at a payload located at a latitude with a cut-off rigidity equal to 1.4 GV. At the same time, no transient effects were seen in any of these parameters by a more equatorially located payload at a latitude with a cut-off rigidity equal to 2.8 GV. The vertical current density at the poleward most payload was enhanced by over a factor of two, for at least 20 min, while the equatorward payload saw no variations. Since these current perturbation times were on the order of the quoted global circuit time constant, and since no variation was seen at the low latitude payload, it was concluded that the global circuit return current may not have been constant through the event.

According to Sheftel et al. (1994), the concept of an atmospheric electricity response to intensive solar flares can be divided into at least three components. The first one is the response to the Forbush decrease of the GCRs flux, the second is the response to an increase of the solar proton flux during a GLE, and the third is the response to a change of cosmic ray geomagnetic cut-off rigidity during magnetic storms conditioned by the flare. Each of these disturbances has its distinctive features, and every real event is the complicated superposition of these disturbances.

Farrell and Desch (2002) suggested that SEPs ($\mathcal{E} > 100$ MeV) can affect the fair-weather electric field at ground level. They created a model that applies changes in the high-altitude atmospheric conductivity profile to the GEC. They found that the strongest flare-generated proton events are capable of creating a measurable change to the electric field at ground level (5% change), but these changes are small in comparison to those associated with passing thunderstorms.

Kokorowski et al. (2006) presented in-situ atmospheric electricity measurements during the highly energetic GLE event on January 20, 2005, taken at the MINIS stratospheric balloon campaign above Antarctica. One-to-one increases in the electrical conductivity and decreases to near zero of both the vertical and horizontal electric field components were observed in the stratosphere, in conjunction with an increase in particle flux at GLE onset. Rapid vertical electric field changes were observed many hours later. These two unique features of the MINIS data set cannot be explained by simply enhancing the atmospheric conductivity. Instead, the rapid vertical fluctuations are likely related to rigidity cut-off motion, while the vanishing of the horizontal field may be connected to more interesting magnetospheric dynamics.

Harrison and Usoskin (2010) compared surface vertical current density and electric field magnitude measurements made independently at Lerwick Observatory, Shetland, from 1978 to 1985, with modeled changes in cosmic ray ionization arising from solar activity changes. Both the lower troposphere atmospheric electricity quantities were found to significantly increase at CR maximum (solar minimum), with a proportional change more pronounced than that of the CR variation. The percentage change between the CR maximum and minimum was 5.4% for neutron monitor (NM) counts, 12% for the electric field magnitude, and 16.5% for the current density magnitude. Additionally, 10% change in NM count resulted in a 15.4% change in IP, consistent with the correlation of Markson (1981).

Nicoll and Harrison (2014) presented simultaneous measurements of increased ionization in the troposphere, with a response in surface atmospheric electrical parameters at a mid-latitude site during a SEP event associated with a solar flare on April 11, 2013. The vertical ionization rate profile obtained using a balloon-borne detector showed enhanced ionization with a 26% increase at 20 km over Reading, United Kingdom. Fluctuations in atmospheric electrical parameters were also detected beneath the balloon's trajectory at the surface. The absence of geomagnetic fluctuations allowed the electrical variations to be attributed solely to ionization effects. During this event, the lack of response of surface NMs indicated that energetic particles that are not detected at the surface by NMs could nevertheless enter and influence the atmosphere's weather-generating regions.

Elhalel et al. (2014) examined the temporal variations and spectral characteristics of continuous measurements of vertical current density, conducted at the Wise Observatory in Mitzpe-Ramon, Israel, during two large CMEs, and during periods of increased solar wind density. Evidence was presented for the effects of geomagnetic storms and substorms on low latitude vertical current density during two CMEs, on October 24—25, 2011 and March 7—8, 2012, when the variability in current density increased by an order of magnitude compared to normal fair weather conditions. Similar low-frequency characteristics occurred during periods of enhanced solar wind proton density.

Jánský and Pasko (2015) used a time-dependent 3D spherical model of GEC to model the effects of conductivity perturbations appearing in the middle atmosphere, produced by γ ray bursts from magnetars. These perturbations have timescales between 0.01–10 s. They found the modification of the IP to be minor. Increasing the conductivity by a factor of 10 at altitudes above 20 km, they found that the IP increases (even slightly) if the perturbation is at the same hemisphere with the thunderstorm that acts as a GEC source, decreases if the perturbation is at the opposite hemisphere, and remains constant if the perturbation covers the whole atmosphere. Although the conductivity perturbation was caused by another physical process, their results are applicable in the case of similar conductivity perturbations due to solar activity, because the GEC electrical response depends on resultant perturbations and not on the cause of them. It can be argued that, the timescale of the perturbations due to the γ ray bursts are much smaller than of the perturbations due to the GLEs, and therefore, the GEC response can be different. As Holzworth et al. (1987) pointed out, the GEC time constant can be large enough, meaning that both phenomena can create transient perturbations, much faster than the GEC relaxation time, and consequently lead to qualitatively similar results.

Slyunyaev et al. (2015) analyzed and discussed the sensitivity of the GEC to variations of atmospheric conductivity and current sources. The IP variation due to solar activity and, in particular, solar modulation of GCR flux was also discussed and modeled, which required an adequate parameterization of the rate of atmospheric ion-pair production over the solar cycle. It was estimated that the maximum IP variation on the

scale of the solar cycle does not exceed 5% of the mean value unless source current perturbations are taken into account.

Tacza et al. (2018) investigated the effect of solar events on the GEC by analyzing the atmospheric electric field variations in fair weather regions. No significant effect was found during solar flares without solar protons, suggesting that solar flare photons are unlikely to modify the GEC. Intense SEPs may modify the conductivity in areas above thunderstorms (disturbed weather regions), affecting the GEC in fair weather regions. Furthermore, a very intense SEP event (which occurred together with GLE71) can produce changes in the ionization which modifies the atmospheric conductivity and, therefore, alters the atmospheric electric field on the Earth's surface in fair weather regions. We note that the acronym GLE71 corresponds to the 71st GLE event registered since 1942. Moreover, throughout the rest of the manuscript, the acronym GLEXX (where XX a number) refers to the XX GLE event recorded since 1942.

Motivated by the studies mentioned above, we focus on the study of GLE events on atmospheric electrical properties, in fair weather and in the presence of aerosols, such as dust particles, and on the dust particle electrification mechanism of ion attachment. This can be seen as a novel effort for the quantification of solar activity with the dynamics of atmospheric particles. We use the 1D numerical model developed by Mallios et al. (2021b), for the study of spherical dust particle electrification and settling in the presence of large scale electric field.

The model takes into account several atmospheric processes, such as: (i) the ionization due to the cosmic rays radiation, (ii) the ion–ion recombination, and (iii) the ion attachment to dust particles, and can calculate self consistently the modification of the atmospheric ion densities in the presence of the dust particles, and the consequent alteration of the atmospheric electrical conductivity and the large scale electric field. Moreover, it can evaluate the acquired electrical charge on the dust particles and thus calculate the electrical force that is applied to them. Finally, the effect of the electrical force on the gravitational settling, and the terminal velocity is quantified. By modifying the ionization rate, the effects of the GLE events in local atmospheric electricity parameters can be studied and quantified. This study constitutes the first step and serves as proof of concept, highlighting and quantifying the coupling of the solar activity-atmospheric electrical properties. It can be considered as a first step towards a global model, that would be able to account for horizontal asymmetries and inhomogeneities and quantify this coupling on a global scale.

In Section 2 the mathematical formulation of the model along with all the assumptions and considerations is presented and explain. In Section 3 the results of the model under different conditions are presented and discussed. Finally, in Section 4 the results of this work are summarized.

2. Model formulation

2.1. System dynamics

The system dynamics have been presented and discussed thoroughly by Mallios et al. (2021b). The bottom ($z = 0$ km, Earth's surface) and the top ($z = 40$ km) boundaries are assumed to be perfect conductors of electricity. At the bottom boundary, the electrical potential, Φ, is set equal to 0 V, while at the top boundary is a parameter under examination.

In the region under investigation, the ion conductivity is dominant over the electron conductivity, as electron number density exceeds the bipolar ion number densities at altitudes above ~60 km (Pasko et al., 1997). Therefore, the particle types considered in the presented formalism are the small atmospheric ions and the dust particles in terms of atmospheric aerosol content.

The mineral dust particles are assumed to be spherical with mass density, ϱ_p, and good conductors of electricity. The large electrical

conductivity can be explained by the water adsorption that takes place on the particle surface at low electric field frequencies and even at low humidity (e.g. Ulanowski et al., 2007, and references therein).

The wind speed has been neglected, and the particle velocity with respect to the air is the same as the particle velocity with respect to an observer at the ground, $\vec{v}_p$.

The continuity equation for positive and negative small ion number densities, $n^\pm$, is:

$$\frac{dn^\pm}{dt} = -\vec{\nabla} \cdot \left[\pm n^\pm \mu^\pm \vec{E} - D_{\text{ion}}^\pm \vec{\nabla} n^\pm \right] + q - an^+ n^- - n^\pm \sum_i \beta_i^\pm, \tag{1}$$

where $\mu^\pm$ are the positive and negative small ion electrical mobilities, $\vec{E}$ is the large scale electric field, $D_{\text{ion}}^\pm$ are the positive and negative small ion diffusion coefficients, q is the ion pair production rate, a is the ion–ion recombination rate, and $\beta_i^\pm$ are the positive and negative ion attachment rates to dust particles with radius r_i. The first two terms in brackets are the flux of small ions due to their motion in response to the large-scale electric field and the ionic diffusion. The third term describes the production rate of positive and negative ions, while the last two terms express the ion losses due to recombination and attachment to dust particles.

The current continuity equation for the charge transport of dust particles with radius r_i is:

$$\frac{d\rho_{p,i}}{dt} = -\vec{\nabla} \cdot \left[\rho_{p,i} \vec{v}_{p,i} - D_{p,i} \vec{\nabla} \rho_{p,i} \right] + q_e \left(\beta_i^+ n^+ - \beta_i^- n^- \right), \tag{2}$$

where $\rho_{p,i}$ is the dust particle charge density, $\vec{v}_{p,i}$ is the dust particle velocity, $D_{p,i}$ is the dust particle diffusion coefficient, and q_e is the elementary charge. We note that all physical constants appearing in the manuscript are listed in Table A.1 in Appendix A. The first two terms in brackets are the charge flux due to the dust particles advection/settling (advection is a valid term for the 3D case where horizontal components of velocity exist, while the settling happens in the 1D case, where the particles fall in the vertical direction), and the diffusion. The third term describes the gain of charge due to the ion attachment.

The continuity equation for the transport of number densities, $N_{p,i}$, that correspond to dust particles with radius r_i, is:

$$\frac{dN_{p,i}}{dt} = -\vec{\nabla} \cdot \left[N_{p,i} \vec{v}_{p,i} - D_{p,i} \vec{\nabla} N_{p,i} \right], \tag{3}$$

where the terms in brackets are the dust particle flux due to the advection/settling and the diffusion.

Finally, the large scale electric field, $\vec{E}$, is calculated from the total charge density, ρ_{tot}, from the Gauss law:

$$\vec{\nabla} \cdot \vec{E} = \frac{\rho_{\text{tot}}}{\varepsilon_0} = \frac{\sum_i \rho_{p,i} + q_e \left(n^+ - n^- \right)}{\varepsilon_0}. \tag{4}$$

Although Eqs. (1)–(4) are generic, we focus on the 1D case, in the vertical direction along the altitude. The applicability of the model can be easily extended to other types of aerosols that can be simulated by spherical shapes and act as good conductors of electricity, but this is beyond the scope of the current work.

Substituting $\vec{E}$ in Eq. (4) with $-\vec{\nabla}\Phi$, the Poisson equation is derived, which is solved using a Full Multigrid Algorithm (FMG) (Press et al., 1992, p. 877). The advection terms in Eqs. (1)–(3) are discretized using the third order Upstream Nonoscillatory (UNO3) advection scheme (Li, 2008). The diffusion terms in Eqs. (1)–(3) are discretized as a second order central difference scheme.

Extensive details on the formulation of the parameters used in Eqs. (1)–(4), can be found in Mallios et al. (2021b).

2.2. Meteorological conditions

The U.S. Standard Atmosphere 1976 (NOAA/NASA/USAF, 1976) is considered as the standard static atmospheric model, and the vertical distributions of pressure, P, and temperature, T, are constant over time
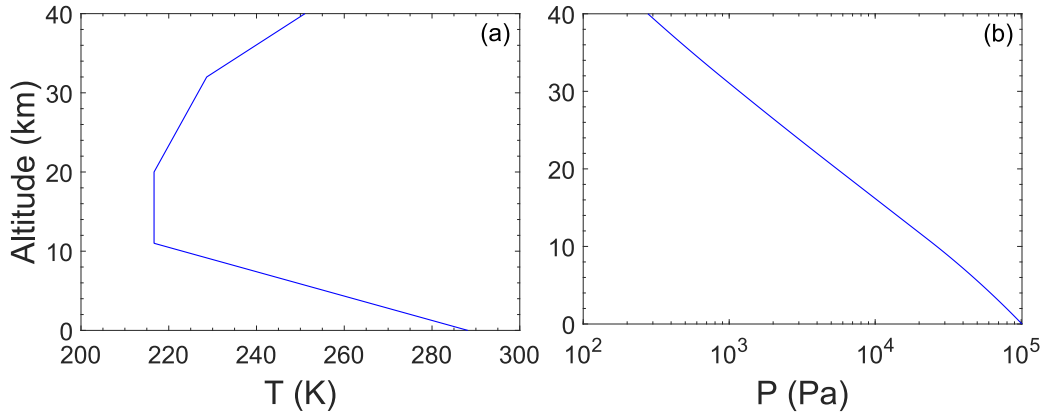
Fig. 1. Vertical distribution of the meteorological parameters in SATP: **(a)** temperature T, and **(b)** pressure P.
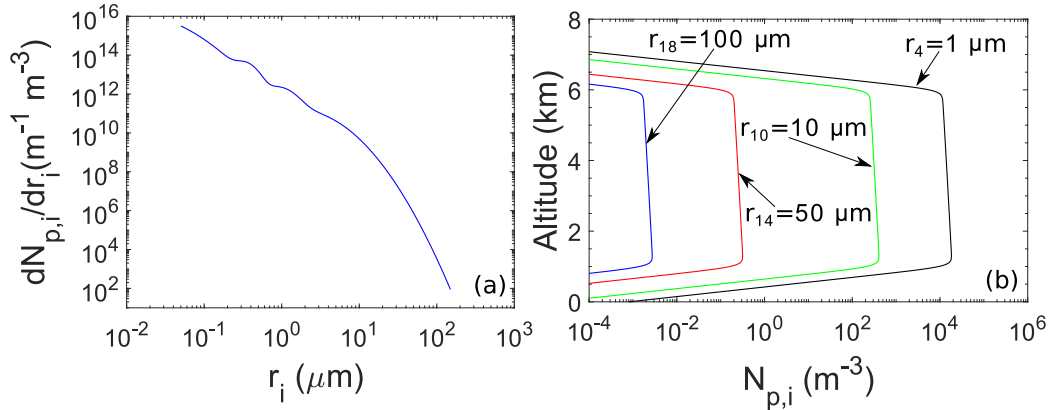
Fig. 2. Particle number density distributions: **(a)** measured mean normalized number density distribution by Ryder et al. (2013b), **(b)** vertical profile of number density distribution, $N_{p,i}$, along the altitude.

(see Fig. 1). The air mass density, ϱ_{air}, at a given altitude can be calculated from pressure and temperature, provided that the atmosphere is an ideal gas:

$$\varrho_{air} = \frac{P}{R^*T}, \tag{5}$$

where R^* is the specific gas constant for dry air.

2.3. Dust particle number density distribution

The mean size distribution between altitudes of 1–6 km at STP, measured by Ryder et al. (2013b) during the Fennec 2011 aircraft campaign at Mauritania and Mali, is used as the dust particle size distribution (Fig. 2a). The adopted size distribution is discretized using 19 bins, similarly to Mallios et al. (2021b), and listed in Table B.1 in Appendix B.

In reality, this distribution is valid near the emission sources, but it decreases in regions away from the emission sites due to the dust particle settling. Since one of the scopes of the current work is to study the effects of GLEs on the dynamics of an atmospheric sub system such as the dust particle settling, the measured average size distribution is used as a generic initial distribution in the model, to highlight the coupling mechanism between different systems and processes. A more comprehensive study on more "realistic" dust particle size distributions is planned to be made in future publications, along with the proper modeling of the dust particle transport in the framework of a 3d model.

The dust particles are introduced in the simulation domain as a rectangular distribution along with the altitude (Fig. 2b):

$$N_{p,i} = \frac{1}{2} N_{0,i} \left(\frac{273.2}{T} \right) \left(\frac{P}{101320} \right) \begin{cases} \left[1 - \tanh \left(\frac{z - h_i - \frac{d_i}{2}}{b_z} \right) \right] & , z \geq h_i \\ \left[1 - \tanh \left(\frac{-d_i}{2b_z} \right) \right] & , z < h_i \end{cases}, \tag{6}$$

where $h_i = 3$ km is the altitude of the distribution center, $d_i = 2500$ m is the distribution depth, and $b_z = 3d_z$ is a smoothing factor regarding the number of mesh points that will sample the boundary of the distribution (in our case 3). The two terms right before the bracket convert the number density $N_{0,i}$ from STP to the model ambient temperature and pressure conditions at a given altitude, z.

2.4. Ionization rate

In general, the cosmic-ray induced ionization rate, q_{CR}, is given by Usoskin and Kovaltsov (2006):

$$q_{CR}(\phi, P_c, x) = \sum_i \int_{\mathcal{E}_{c,i}(P_c)}^{\infty} J_i(\phi, \mathcal{E}) Y_i(\mathcal{E}, x) d\mathcal{E}$$
$$= \sum_i \int_{\mathcal{E}_{c,i}(P_c)}^{\infty} J_i(\phi, \mathcal{E}) \left(\frac{\alpha}{\mathcal{E}_{ion}} \frac{\Delta \mathcal{E}_i}{\Delta x} \right) d\mathcal{E} \tag{7}$$

where ϕ is the modulation potential (a direct measure of solar activity given in MV), P_c is the geomagnetic cut-off rigidity, and x is the atmospheric depth. For primary cosmic ray particle with index i, $\mathcal{E}_{c,i}(P_c)$ is the kinetic energy corresponding to the local P_c, $J_i(\phi, \mathcal{E})$ the differential cosmic ray particle flux at Earth, $Y_i(\mathcal{E}, x)$ the atmospheric ionization yield function, and $\mathcal{E}$ is the particle's kinetic energy (given in MeV/nuc). The parameter $\alpha = 2\pi \int \cos(\theta) \sin(\theta) d\theta$ is the geometrical

normalizing factor (θ being the zenith angle varying between 0° and 90°). Moreover, $\mathcal{E}_{\mathrm{ion}} \approx 32$ eV (e.g., Wedlund et al., 2011) is the average atmospheric ionization energy, and $\Delta\mathcal{E}_i$ the mean specific energy loss at a certain atmospheric depth Δx. Thus, the total CR-induced ionization rates strongly depend on the solar activity, through ϕ, the geographic location, which alters P_c, and the altitude, that depends on the atmospheric depth, x.

The influence of the modulation of GCRs can be studied with the help of the often-used Force-Field approximation (Caballero-Lopez and Moraal, 2004):

$$J_i(\mathcal{E}, \phi) = J_{\mathrm{LIS},i}(\mathcal{E} + \phi)\frac{\mathcal{E}(\mathcal{E} + 2\mathcal{E}_r)}{(\mathcal{E} + \Phi_i)(\mathcal{E} + \Phi_i + 2\mathcal{E}_r)}, \tag{8}$$

where $J_{\mathrm{LIS},i}$ represents the unmodulated local interstellar spectrum of ith species (here we use the LIS by Herbst et al., 2017), and $\mathcal{E}_r = 938$ MeV/nuc denotes the rest energy of the primary particle. The solar modulation function of ith species is given by $\Phi_i = (Z_i q_e / A_i)\, \phi$, with Z_i being the atomic number, and A_i the mass number of the particle.

The geomagnetic cut-off rigidity P_c is a direct measure for the ability of a charged particle to enter the magnetic field at a certain location and is used to both describe the shielding effect of the geomagnetic field and to order charged particle data acquired in the magnetosphere (Smart and Shea, 2005). P_c can, e.g., be derived by Størmer's approximation (Elsasser et al., 1956) as:

$$P_c \approx 1.9\ M \cos^4 \varphi_G, \tag{9}$$

where φ_G is the geomagnetic latitude, and M is the dipole moment of the geomagnetic field, expressed in 10^{22} Am^2. The geomagnetic latitude depends on the geographic latitude and longitude and the Earth's geomagnetic north pole position. We note that Eq. (9) provides a reasonable first-order approximation to the effective cut-off rigidity for isotropic flux (Cooke, 1983). However, other cut-off rigidity estimates based on, e.g., PLANETOCOSMICS simulations (e.g., Herbst et al., 2013) may lead to differences in the calculated P_c-values, and, thus, the ionization rates. Investigating these differences exceeds the scope of this study and will be addressed soon.

To investigate the impact of CRs on atmospheric electric properties besides GCRs, we have further studied two GLEs. We investigated the impact of GLE05, the largest GLE directly measured so far, that occurred on February 23, 1956 ($\phi = 589$ MV, $M_{05} = 8.05 \times 10^{22}$ Am^2) and GLE59 that occurred on July 14, 2000 ($\phi = 1220$ MV, $M_{59} = 7.79 \times 10^{22}$ Am^2). Both ϕ-values have been derived based on Usoskin et al. (2011) and Herbst et al. (2017).[1]

GLE05 was measured on February 23, 1956 by 14 NMs around the world (Table C.2). Although there were no in-situ spacecraft measurements of the solar wind nor complementary solar data (i.e., X-rays, CMEs), the magnitude of the event ~5120% increase in Leeds NM (cut-off rigidity ~2.2 GV, sea-level NM) is remarkable (Belov et al., 2005). Such magnitude led GLE05 to achieve a > 1 GV fluence ~2.5 times larger from an episode of five strong GLEs from August through October 1989 (Cliver et al., 2020) and has one of the hardest spectra among GLEs to date (Asvestari et al., 2017; Usoskin et al., 2020b). The importance of this landmark event and this outstanding period were summarized at that time in Nature (Ellison, 1957) and has been the basis for the quantification of extreme solar events unleashed by our host star in the past (i.e., AD 774/775 SEP event) (Cliver et al., 2020).

GLE59 was recorded by almost ~30 NMs worldwide on July 14, 2000 (Table C.1). A maximum increase of 57.93% was marked at South Pole NM (vertical cut-off ~0.1 GV, altitude = 2820 m) (Belov et al., 2001). A solar flare of X5.7 class and a fast (1674 km/s) and halo

CME were the drivers of this GLE. The most remarkable feature of this event is the high-speed propagation of the CME in the interplanetary space that lasted only ~28 h, signifying the arrival of one of the most impacting CMEs (Török et al., 2018).

In this study, we focus on locations within 5°W to 26°E and 20°N to 65°N, covering regions from the Sahara desert up to Scandinavia. There are several reports in the past, that dust particles can travel from the Sahara desert through this region, reaching the Balkans, central Europe, even Iceland (e.g. Đorđević et al., 2019; Varga et al., 2021). Choosing pairs of latitudes and longitudes lying within the given region, the geomagnetic cut-off rigidities (P_c) given the geomagnetic field dipole moment and Eq. (9) can be derived.

Fig. 3a illustrates the dependence of P_c on the geographic latitude and longitude during the time GLE59 occurred (a similar plot can be derived for GLE05). It can be seen that the dependence on latitude increases as P_c increases. High cut-off rigidity values mean that the shielding effect of the geomagnetic field is stronger, and therefore a large number of charged particles are deflected, reducing the effect on the atmospheric ionization. On the other hand, for small values of P_c, where the dependence on longitude is not significant, the shielding is weaker, leading to a larger contribution of incoming charged particles to the atmospheric ionization. Based on this, and in order to simplify the studied cases, the values of P_c are averaged along with the longitudinal range of 5°W–26°E, for each event, resulting in the latitudinal dependence displayed in Fig. 3b. In addition, Fig. 3c, a geographical representation of regions with the same values of cut-off rigidity is illustrated, focusing on P_c values between 1 and 6 GV.

Fig. 4 depicts the time profiles of the two GLEs under study. The 5-min de-trended NM data have been used since those provide a much more realistic representation of the GLE in the respective NM measurements (see details in Usoskin et al., 2020a). NM stations presented in Fig. 4 for GLE05 span from P_c ~ 1–8 GV with the lowest vertical cut-off rigidity being at Ottawa (OTWA) NM (red line) and the highest one at Mexico (MXCO) NM (black line). GLE59 spans from P_c ~ 0.1–3 GV with the lowest vertical cut-off at the South Pole (SOPO) NM (red line) and the higher vertical cut-off at Moscow (MOSC) NM (black line). The presence of an enhancement up to ~8 and ~3 GV, respectively for each of the two GLE cases, indicate the presence of particles with at least such rigidities, per case.[2] Therefore, a conservative upper limit of 6 GV has been chosen for GLE05 and of 3 GV for GLE59.

To model the altitude-dependent cosmic ray-induced ionization rates, we utilized the simulation code AtRIS (Banjac, Herbst, and Heber, 2019). Based on an averaged atmospheric profile of the regional grid assumed in this study utilizing the NRLMSISSE-00 database[3] we first performed simulations of the GCR-induced ionization. Therefore, the FTFP_BERT_HP (hadronic) interaction packages and the standard EM constructor provided by the GEANT4 collaboration have been used. The results are displayed in Fig. 5. The direct correlation between the solar minimum and maximum conditions (different line styles) and geographic location (different coloring) can be seen. While the ionization rates at flight altitudes are roughly up to a factor of two higher during solar minimum conditions, the ionization rates at the Earth's surface only slightly change. Additionally, it becomes evident that the influence of geographic location on the higher-altitude production rates is more prominent during solar minimum conditions (dashed lines). Further, to study the effect of GLE05 and GLE59 on the atmospheric ionization profile, we utilized the proton fluence spectra by Raukunen et al. (2018).

---

[1] Note that the ϕ-values are LIS-model dependent (Herbst et al., 2010; Herbst et al., 2017). According to the linear regressions given in Herbst et al. (2017) $\phi_{\mathrm{HE17}} = 1.025 \cdot \phi_{\mathrm{US11}} + 24.16$, and thus the 551 (1167) MV given by Usoskin et al. (2011) for February 1956 (July 2000) translate to 589 (1220) MV when the LIS by Herbst et al. (2017) is used.

[2] Note that in the case of GLE05, particles have been recorded up to ~13 GV, however our analysis showed that SEPs dominate the differential particle intensity below ~9 GV and thereafter GCRs take over. Since our goal is to illustrate the effect of solar particles we chose to use a limit (i.e. 6 GV) in which the dominance of SEPs is evident.

[3] https://ccmc.gsfc.nasa.gov/modelweb/models/nrlmsise00.php
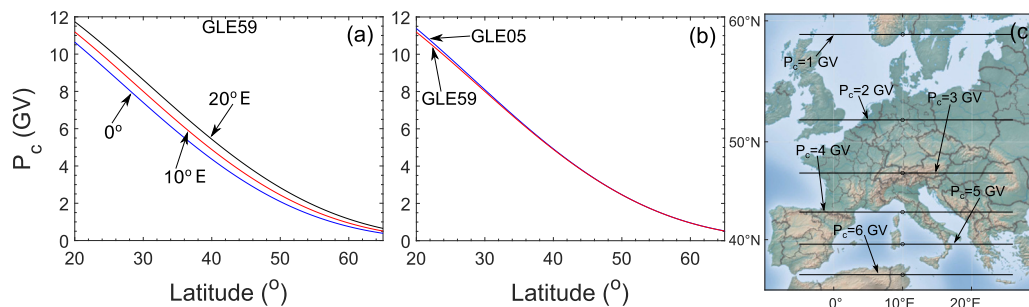
Fig. 3. P_c and geographical location: **(a)** P_c during the GLE59 for different latitudes and longitudes, **(b)** averaged P_c along the longitude, as a function of latitude, for GLE05 and GLE59, **(c)** geographical locations that correspond to values of the same P_c. In circles are the locations investigated in the current work.
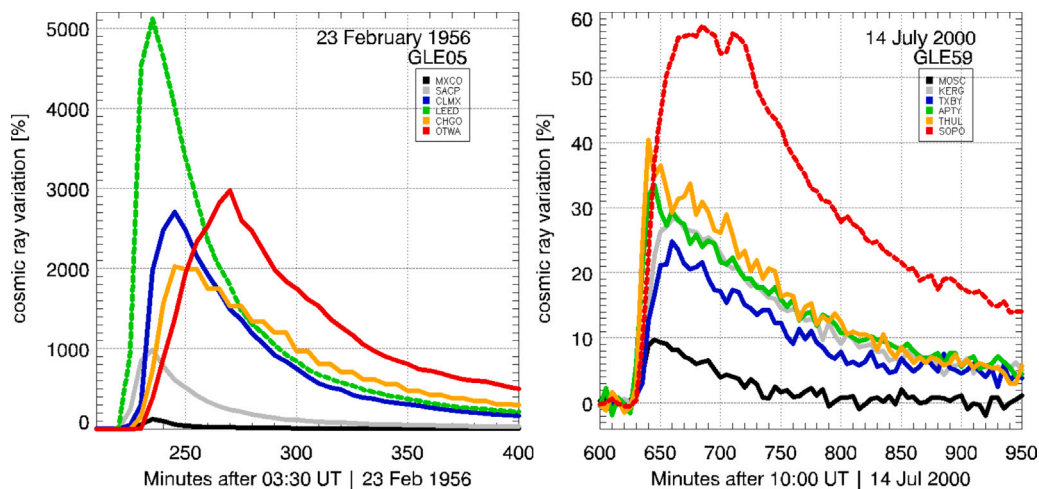
Fig. 4. The time profile and relative increase (%) of cosmic rays recorded by several NMs based on 5-min de-trended NM data; (left panel) GLE05 on 23 February 1956 and (right panel) GLE59 on 14 July 2000.
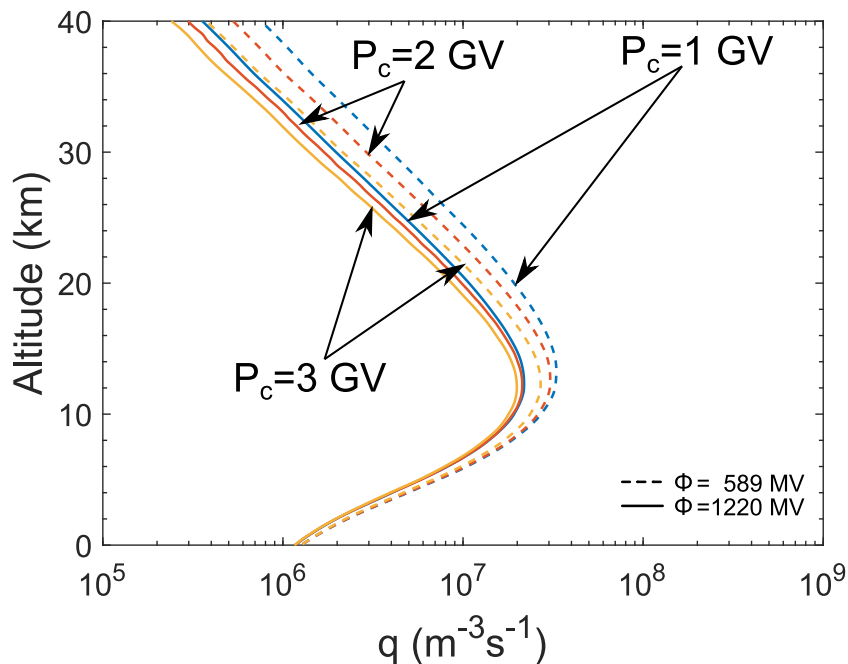
Fig. 5. Galactic cosmic ray induced ion-pair production rates during solar minimum ($\phi = 589$ MV, dashed lines) and maximum ($\phi = 1220$ MV, solid lines) conditions.
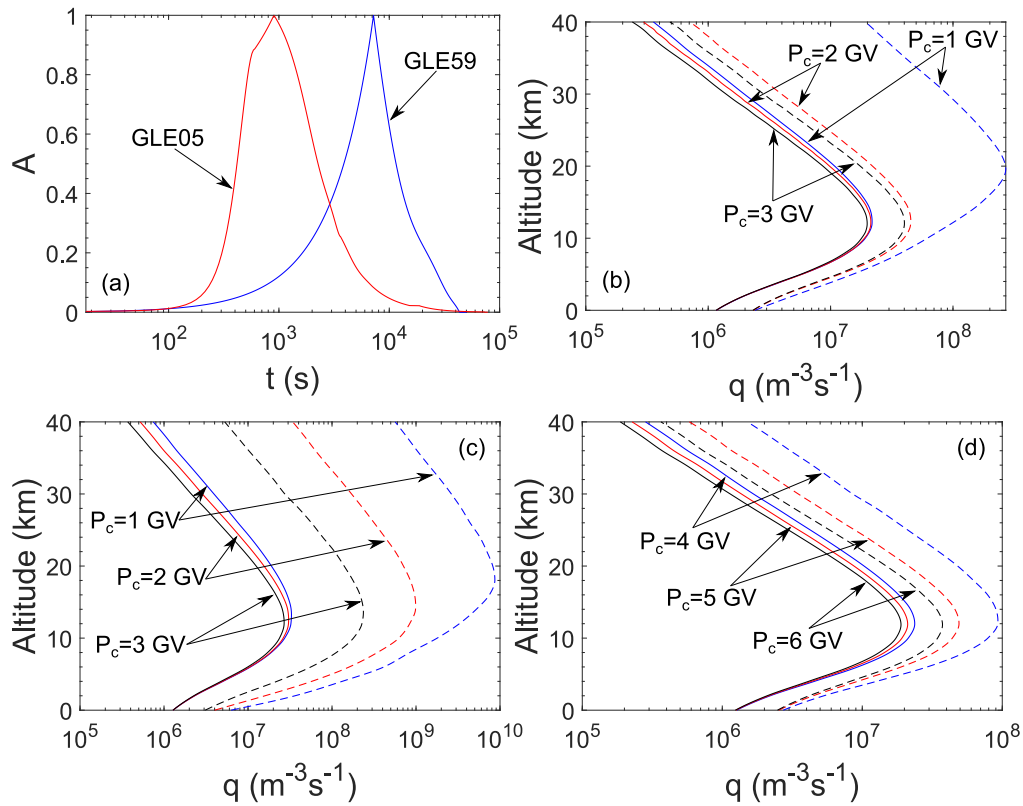
Fig. 6. Ionization rate, q: **(a)** factor A for the temporal contribution of the GLE events on the ionization rate, **(b)** ionization rate along the altitude for the cut-off rigidity values used in the present study, regarding GLE59, **(c)** ionization rate along the altitude for the cut-off rigidity values 1, 2, 3 used in the present study, regarding GLE05, and **(d)** ionization rate along the altitude for the cut-off rigidity values 4, 5, 6 used in the present study, regarding GLE05. The solid lines represent the ionization rate due to the GCR, while the dashed lines denote the total ionization rate at the peak of the GLE event.

In order to clearly identify the contribution of each of the GCR and SEP components we employed a simplified, yet straightforward procedure detailed here below. In particular, we assume that the total ionization rate q is given by:

$$q = q_{GCR} + A \cdot q_{GLE}, \tag{10}$$

where q_{GLE} is the ionization rate caused by the solar particles at the peak of the event, and A is a factor that illustrates the temporal contribution of the GLE event to the total ionization rate. As shown in Fig. 6a, in the beginning of the event A is zero and the ionization rate depends only on the GCR contribution, while at the peak of the event ($A = 1$) the contribution of the GLE has reached its maximum. Thereafter A decreases to zero at the end of the event.

We note that A results from a fitting procedure based on the GLE measurements from the NMs that had the most prominent peak per event. Namely, we used the Leeds (GLE05) and South Pole (GLE59) NM peak (Fig. 4). We found that GLE05 rises faster than GLE59 and relaxes slower to the background NM count rates dominated by GCRs. Thus, besides the steeper energy spectrum with higher primary particle energies, its contribution to the atmospheric ionization lasts longer than the contribution of GLE59, see Fig. 6(a).

Fig. 6(b) shows the background ionization rate (solid lines), and the total ionization rate at the peak of GLE59 (dashed lines) for P_c between 1 GV and 3 GV. In the case of $P_c = 1$ GV, the ionization rate increases more than one order of magnitude compared to the background value, while in the case of $P_c = 2$ GV the increase does not exceed a factor of three. It further shows that the larger contribution of the GLE event occurs at high altitudes, from the stratosphere and above. At altitudes below 10 km (in the troposphere) the increase of the ionization rate due to the GLE event is almost independent of the cut-off rigidity, and does not exceed a factor of two.

Figs. 6(c) and 6(d) show the impact of GLE05 on the atmospheric ionization at location with R_c between 1–3 GV and 4–6 GV, respectively. As in Fig. 6c, solid lines give the GCR-induced rates, while dashed lines represent the GLE contribution. As can be seen, at high latitudes ($R_c = 1$ GV), the ionization rates increase by almost two orders of magnitude above 10 km — also, the ionization rates at the surface increase by up to a factor of four. Even at locations with ($R_c = 6$ GV), the ionization rates are increased by almost a factor of two throughout the atmosphere.

However, we note that no other sources of ionization are assumed in the present formulation. Especially the ionization due to the natural radioactivity originating in continental areas, which is the dominant mechanism of ionization in the planetary boundary layer, about 1 km above the ground, (Tinsley and Zhou, 2006) has been neglected for simplicity and the better presentation of the mechanism under investigation.

2.5. Ionospheric potential

Markson (1981) reported a positive correlation between the cosmic radiation recorded by the NM at Mount Washington, New Hampshire, and simultaneous (within an hour interval) IP measurements, using least squares regression. Two data sets of potential measurements were used. The first one was obtained in the Bahamas using an aircraft from December 1971–March 1972, during the declining phase of solar cycle 20 (Markson, 1976). The correlation of this data set with the NM measurements showed that the 10% increase of the cosmic radiation resulted in a 22% increase of the IP.

The second data set contained a more significant number of measurements and was obtained by balloon soundings in Germany between 1959 and 1976, during the declining phase of solar cycle 19 and the complete solar cycle 20 (Fischer and Mühleisen, 1980). In this case, a

10% increase of the cosmic radiation resulted in a 13%–14% increase of the IP. The differences between the correlations are attributed to the different periods of the Bahama data (3 months) compared with the German data (17 years) (Markson, 1981). Additionally, these differences can be attributed to the differences in the solar cycle phase that each data were obtained.

Although it is emphasized by Markson (1981) that the percent increase of the IP with 10% increases in cosmic radiation should not be interpreted quantitatively, but rather as estimates of the expected responses range, it is clear that the ratio of the IP change to cosmic ray change (as reflected by NM count rate change) is greater than unity, and therefore observations suggest that, the IP can change during solar activity.

The physical mechanism that justifies this modification is still not clear. Markson (1978) proposed that the ionization increase above thunderstorms, enhances the ion densities, and consequently the electrical conductivity:

$$\sigma = q_e \left(n^+ \mu^+ + n^- \mu^- \right). \tag{11}$$

Defining the conduction current density as:

$$\vec{J} = \sigma \vec{E}, \tag{12}$$

increase of the conductivity amplifies the conduction current (assuming that the generated electric field magnitude inside the thunderstorms does not change). Since thunderstorms are considered the main contributors to the IP, amplifying their output current leads to amplifying the IP.

Slyunyaev et al. (2015) used a simple equivalent-circuit model and presented a general discussion of the IP sensitivity to atmospheric electrical conductivity and source current perturbations. They pointed out that the Markson (1978) proposed mechanism holds if the thunderstorms are considered voltage sources of the GEC. If thunderstorms are considered current sources, amplifying the IP requires the conductivity reduction inside the thunderstorms. This generally happens due to the ion attachment to cloud particles (Gunn, 1954, 1956). Additionally, it is required for the conductivity to remain unchanged below the thunderstorms, which is not the case since enhancement of the ionization occurs at all altitudes, even below thunderstorms and right above the ground (e.g. Tinsley and Zhou, 2006).

Additionally, Slyunyaev et al. (2015) showed that under the assumptions that: (1) thunderstorms are current sources of the GEC, (2) the atmospheric electrical conductivity is reduced inside thunderstorms, and (3) the atmospheric electrical conductivity is enhanced below them, the IP is reduced. This is consistent with a global quasi-static model presented by Hays and Roble (1979), where they calculated an increase of the IP when the GCR flux decreases (i.e., during a Forbush decrease) and a decrease of the IP when the SEP flux increases (during a solar flare). These results seem to contradict the measurements and correlations of Markson (1981), but they also contain many uncertainties and are not conclusive.

As Slyunyaev et al. (2015) mentioned, there might be other factors to which the IP is more sensitive, especially those affecting the source current density inside thunderstorms. They also provide an extensive discussion on how the changes of the thunderstorms considerations in numerical models (such as the thunderstorm global spatial distribution and number, whether all thunderstorms are identical or have different electrical behavior, etc.) can change the simulated results. On top of this discussion, we would like to add the fact that these global models require the GEC to be in a steady-state, which can be the case of the slow varying effects of the solar cycle, but not for the solar transient phenomena such as GLEs, or solar flares that last a few hours (Holzworth et al., 1987). Moreover, as has been shown by Jánský and Pasko (2015) the location of the conductivity perturbations with respect to the thunderstorms can also influence the behavior of the IP.

In the current work, we study two scenarios for the IP. The first one is that the potential does not change during the event and is equal to 250 kV, which can be seen as the average potential along the ionosphere (Rycroft et al., 2000). The second scenario is a generalization of Markson (1981) correlations. It is assumed that any increase of the NM counts coexists with increased IP. The ratio of the IP change (with respect to the constant value of 250 kV) to cosmic radiation change (as observed by NMs with respect to the baseline value) is considered to be equal to 1.3, which is consistent with the correlation results based on the German data set.

For the calculation of the IP change during the two GLE events the following procedure is followed: The available NMs during each event are identified based on data obtained from the GLE database (https://gle.oulu.fi/), and are shown in Figs. 7a and 7d. The latitude range 90°N–90°S, and the longitude range 180°W–180°E, are discretized in points with step 1°. At each point the cut-off rigidity, P_c is calculated (Figs. 7b and 7e), based on Eq. (9).

At points with $P_c > P_{c,\lim}$, the percentage increase is set equal to zero. $P_{c,\lim}$ is the upper energy limit of the GLE event particles, which are shielded completely by the Earth's magnetic field in regions with cut-off rigidity above this value. A conservative upper limit of $P_{c,\lim} = 3$ GV was used for GLE59 and, $P_{c,\lim} = 6$ GV for GLE05 (see Fig. 4). At the rest of the points, interpolation has been performed based on the inverse distance weighting algorithm (Shepards's algorithm, Shepard, 1968), taking into account the points that were set equal to zero and the values from the NMs (the percentage increase that each available NM recorded at the peak of each GLE event, with respect to its baseline, is listed in Tables C.1 and C.2 in Appendix C). The distance between two points required by the interpolation algorithm is calculated using the haversine formula (Gade, 2010), under the assumption of a spherical Earth with a mean radius of 3671 km. Moreover, the power parameter used in the interpolation algorithm that regulates the influence of values closest to the interpolated point is set to a value above which the average over the whole map converges to a specific value. In the case of GLE59, the power parameter is set equal to 30, while in the case of GLE05, the power parameter is set equal to 45.

Figs. 7c and 7f illustrate the interpolated values all over the map for GLE59 and GLE05, respectively. These values would estimate the percentage increase that could have been recorded if a NMs existed at each point. These values depend on the number of NMs used in the interpolation procedure, but they seem to be physically reasonable results. The maximum increase appears at the poles that have very low cut-off rigidity values, while there is no increase between 45°N–45°S latitudes where the rigidity is maximized. In the case of GLE05, due to the small number of available NMs, especially in the southern hemisphere, the interpolated values can be considered as an underestimation of the "actual expected" values.

Multiplying the results of Figs. 7c and 7f with the factor 1.3, the percentage increase of the IP can be found at each location. In the case of GLE59, the maximum percentage increase is 75.3%, while in the case of GLE05, it is 6650%. The spatial distribution of the IP seems to contradict that the potential about above 70 km altitude (lower part of the ionosphere, inside the equalization layer) is almost constant, as a consequence of the conductivity anisotropy that makes the conduction current horizontal (Tzur and Roble, 1985). This discrepancy can be attributed to the generalization of the IP-cosmic radiation correlation. Markson (1981) derived the correlation based on a specific NM (Mount Washington, New Hampshire). In reality, each NM records a different count percentage increase with respect to its baseline for the same potential percentage increase (assuming that the IP is spatially constant). This means that each NM station will have a unique IP-cosmic radiation correlation, and more work needs to be done in this direction. In the present study, for the treatment of this issue, the potential percentage increase is averaged along with the whole map, leading to a constant global increase. In the case of GLE59, this increase is 18.6%, while in the case of GLE05, it is 794.2%.
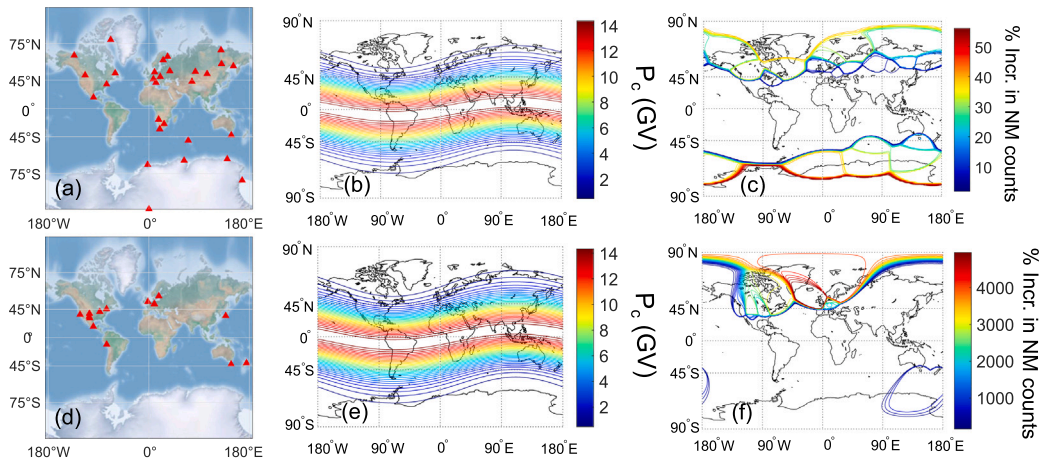
Fig. 7. (a) Location of the NM stations that provided data during the GLE59, **(b)** P_c distribution along the globe during the GLE59, **(c)** interpolated values of the NM station % increase counts at the peak of the GLE59 with respect to the baseline, **(d)** Location of the NM stations that provided data during the GLE05, **(e)** P_c distribution along the globe during the GLE05 **(f)** interpolated values of the NM station % increase counts at the peak of the GLE05 with respect to the baseline.

The temporal variation of the IP (the top boundary of the simulation domain) can be modeled similar to Eq. (10):

$$\Phi_{\mathrm{ion}} = 250 \left[1 + A \frac{\Delta\Phi_\%}{100} \right], \qquad (13)$$

where $\Delta\Phi_\%$ is the percentage increase, and Φ_{ion} is in kV.

2.6. Simulation procedure

At each of the six points illustrated in Fig. 3c, that correspond to different cut-off rigidity values, Eqs. (1)–(4) are solved in the absence of dust particles ($\rho_{p,i} = N_{p,i} = 0$), with $q = q_{GCR}$, and $\Phi_{\mathrm{ion}} = 250$ kV. The calculations carry on, until steady state is reached ($\frac{dn^\pm}{dt} = 0$). The derived distributions along the altitude of $n_{\mathrm{fw}}^\pm$ and $E_{z,\mathrm{fw}}$ form the initial fair weather conditions of each location.

As next step, the time is set $t = 0$ s, the dust particle bins are placed in the domain and are allowed to move according to Eqs. (1)–(4). The ionization rate, q, is expressed by Eq. (10), while the IP either remains constant or is calculated by Eq. (13), depending on the case study. The calculations proceed until the end of each GLE event, $t = 50000$ s for GLE59, and $t = 78000$ s for GLE05. At each time step the ion number densities, $n^\pm$, the electrical potential, Φ, the electric field magnitude, E_z, the dust particle charge densities, $\rho_{p,i}$, the dust particle number densities, $N_{p,i}$, and the dust particle velocity magnitudes, $|\vec{v}|_{p,i}$ are derived.

The average charge of each bin at a given altitude, q_i is calculated by dividing the dust particle charge density, with the dust particle number density, $q_i = \frac{\rho_{p,i}}{N_{p,i}}$. Finally, the electrical force magnitude upon a dust particle of specific size at a given altitude is obtained as $F_{\mathrm{el}} = q_i E_z$.

3. Results and discussion

3.1. Effects of the ionization rate enhancement

First, the IP is kept constant during the GLE events, equal to 250 kV, and the GLE events are assumed to modify only the ionization rate in the atmosphere. This is consistent with the hypothesis that the potential difference between the lower part of the ionosphere and the Earth's surface is generated almost solely by thunderstorms. As a first approximation, it can be considered that the majority of thunderstorms can be distributed between 45°N–45°S (see e.g. Brooks et al., 2003). In this region, the GLE events do not alter the ionization rate due to high rigidity values (Figs. 7b,7c,7e, 7f), and therefore the thunderstorm electrical properties remain unaffected, keeping the IP value constant.

3.1.1. Fair weather electrical properties

The simulation procedure is performed to study the effect of GLEs in the fair-weather electrical properties without introducing dust particles. After calculating the initial fair weather conditions, the ionization rates are modified according to Eq. (10) until the end of the time span covered by the GLEs at each case. Moreover, for the generalization of the results, fair weather conditions are assumed everywhere above 45°N and below 45°S. This means that in these regions, the electric field is vertical, and since here we have vertical electric field, the conclusions drawn by the effect of GLEs on the electrical properties in these regions are assumed to be valid on a global scale.

GLE59 case. Fig. 8a illustrates the altitude-dependent fair weather electrical conductivity distribution for locations with different cut-off rigidity values prior to the occurrence of GLE59. The electrical conductivity monotonically increases, opposed to the ionization rate vertical distribution behavior, and consequently, the ion number density vertical distribution behavior, which rises up to an altitude of ~15 km, and then falls (see Fig. 5). This comes from the fact that the electrical conductivity also depends on the ion electrical mobility distribution (i.e. Eq. (11)), which increases monotonically (e.g. Mallios et al., 2021b, and references therein), and compensates the decrease of the ion density number density.

The electric field magnitude distribution along the altitude is monotonically decreasing (Fig. 8b), resulting from the system's steady state. In the steady-state, the current density along the altitude is constant (which is the steady-state condition inside conductors, see, e.g., Landau and Lifshitz, 1963, p. 86), as can be seen in Fig. 8c. Based on Eq. (12), when the conduction current is constant, increasing conductivity leads to decreasing electric field magnitude.

It is also clear that although the selected locations cover a latitude range between 47°N–59°N, the fair-weather electrical properties, especially in the troposphere, are almost identical. The conduction current magnitude relative difference between locations with $P_c = 1$ GV and $P_c = 3$ GV, is less than 2%.

As GLE59 progresses, the ionization rate increases, leading to an increase of the ion number densities and the atmospheric electrical conductivity. The increase is larger at altitudes from the stratosphere and above (> 12 km), and for locations with $P_c < 2$ GV (Fig. 6b). Fig. 8d illustrates the percentage relative difference between the initial fair-weather conductivity and the conductivity at the peak of the GLE59. In the case of regions with $P_c = 2$–3 GV, the conductivity increase is almost constant along the altitude and lies in the range 30%–40%. On the other hand, in the case of $P_c = 1$ GV, the increase starts from 40% right above the ground and reaches a value of 610% at 40 km altitude.
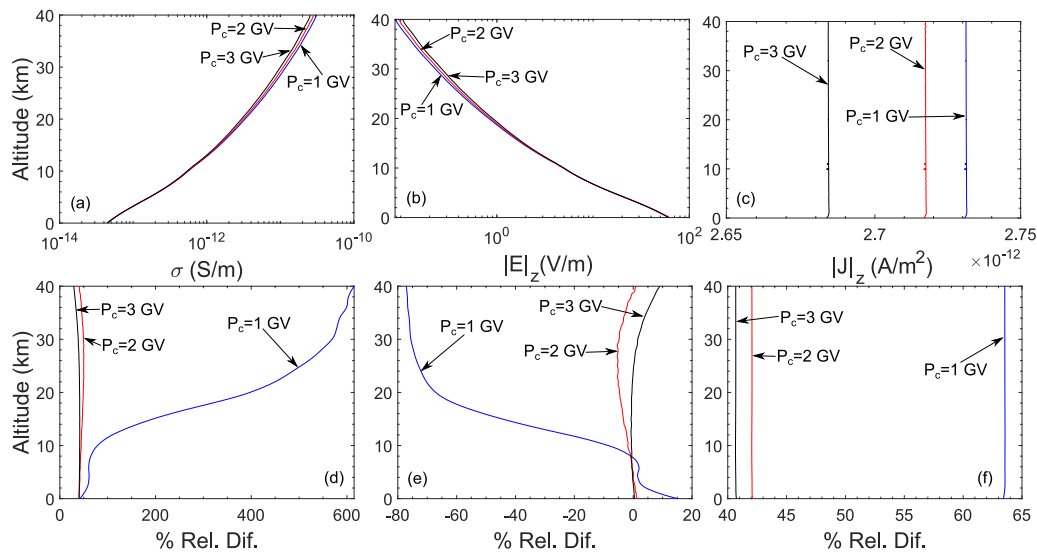
Fig. 8. Electrical properties of the fair weather atmosphere prior and at the peak of GLE59 for locations with different cut-off rigidity value, P_c: **(a)** Conductivity distribution along the altitude prior to event, **(b)** electric field magnitude distribution along the altitude prior to event, **(c)** conduction current density magnitude distribution along the altitude prior to event, **(d)** percentage relative difference between conductivity at the peak of the event and the ambient fair weather value, **(e)** percentage relative difference between electric field magnitude at the peak of the event and the ambient fair weather value, **(f)** percentage relative difference between conduction current density magnitude at the peak of the event and the ambient fair weather value.

Although the system is at a steady-state, as can be seen from Fig. 8f, where the percentage increase of the current density magnitude with respect to the initial value is constant along the altitude, and therefore the current density distribution remains constant, the electric field magnitude does not decrease similarly to the conductivity increase (Fig. 8e). In the case of $P_c = 3$ GV, the electric field magnitude remains almost constant with its initial value up to 30 km altitude and then increases up to 9%. For locations with $P_c = 2$ GV, decrease up to 5% at around 30 km altitude, and then returns to its initial value. Finally, in the case of $P_c = 1$ GV, the electric field magnitude increases up to 15% in the first 7 km altitude and then decreases up to 80% at 40 km altitude.

The reason for this behavior can be explained as follows. Defining the columnar resistance, R_c as (Rycroft et al., 2008):

$$R_c = \int_0^{z_{max}} \frac{dz}{\sigma}, \tag{14}$$

where z_{max} is the altitude of the top boundary of the simulation domain, the current density magnitude at the ground can be written as (Rycroft et al., 2008):

$$J_{z,0} = \sigma_0 E_{z,0} = \frac{\Phi_{ion}}{R_c}. \tag{15}$$

Since the current altitude-dependent density is constant due to the steady-state, the electric field magnitude at any altitude can be written as:

$$J_z = J_{z,0} \Rightarrow E_z = \frac{\Phi_{ion}}{\sigma R_c}. \tag{16}$$

As the conductivity increases, the columnar resistance decreases (Eq. (14)), while the conduction current density magnitude increases (Eq. (16)). This explains the increase of the conduction current density with respect to the initial values (Fig. 8f), as the conductivity increases (Fig. 8d), when the IP, Φ_{ion}, is kept constant. Additionally, from Eq. (16), it is clear that the decrease of the columnar resistance compensates for the increase of the conductivity, and this compensation regulates the increase or the decrease of the electric field magnitude.

For GLE59, the decrease of the columnar resistance at the peak of the event with respect to the initial fair weather value is 28.9% in the case of $P_c = 3$ GV, 29.6% in the case of $P_c = 2$ GV, and 38.8% in the case of $P_c = 1$ GV. The decrease of the columnar resistance in the first two

locations is similar to the increase of the conductivity, which explains the minor modification of the electric field magnitude with respect to its initial value. In the case of $P_c = 1$ GV, though, the decrease of the columnar resistance at altitudes up to 7 km dominates the conductivity increase, leading to enhancement of the electric field magnitude. At altitudes above 7 km, the conductivity increase surpasses the columnar resistance decrease, and the electric field magnitude decreases with respect to the initial fair weather value, as has also been observed by Holzworth and Mozer (1979).

Another interesting point has to do with the IP. At the peak of GLE59 the current density magnitude increases from 40% at 47°N ($P_c = 3$ GV) to 63% at 59°N ($P_c = 1$ GV) with respect to the initial value. The fair weather current during the GLE event increases at least by 40%. Assuming that the system is at steady state, the current driven by the thunderstorms is expected to be equal to the return fair weather current. Since the current sources are assumed to be at regions unaffected by the GLE59, it is concluded that the amplified return fair weather current is a consequence of the constant IP. So, there are two scenarios. (1) The IP should decrease for the equalization between the source and return fair weather current. This is consistent with the model results by Hays and Roble (1979), and Slyunyaev et al. (2015). (2) The system is not in steady state, and there is a temporal difference between the currents, consistent with observations by Holzworth et al. (1987). These scenarios require a more global complex model and are planned to be investigated in the future. A certainty arising from our analysis is that, the GLE events can lead to a significant temporal decrease of the fair weather resistance.

GLE05 case. The same logic is applied in the case of GLE05 (Fig. 9). In this case the decrease of the columnar resistance is more significant compared to the GLE59. It can lead to amplification of the current density magnitude >100%, and enhancement of the electric field in the troposphere >30%, with respect to their initial values, in regions northern than 45°N. Specifically, the columnar resistance decrease is 26.7% for $P_c = 6$ GV, 29.2% for $P_c = 5$ GV, 37% for $P_c = 4$ GV, 48.2% for $P_c = 3$ GV, 63.5% for $P_c = 2$ GV, and 75.1% for $P_c = 1$ GV.

It is also noted that the extensiveness of this event that affects regions between 30°N–45°N leads to possible modification of the current sources' electrical properties. Again, the study of this interaction requires a more extensive model and is planned to be done as a next step.
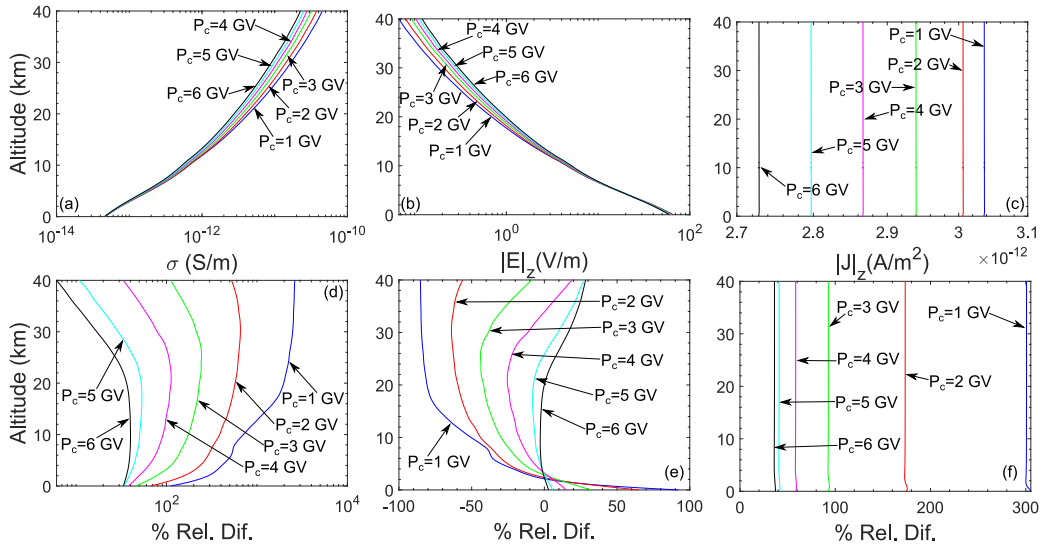
Fig. 9. The same as Fig. 8, but in the case of GLE05.
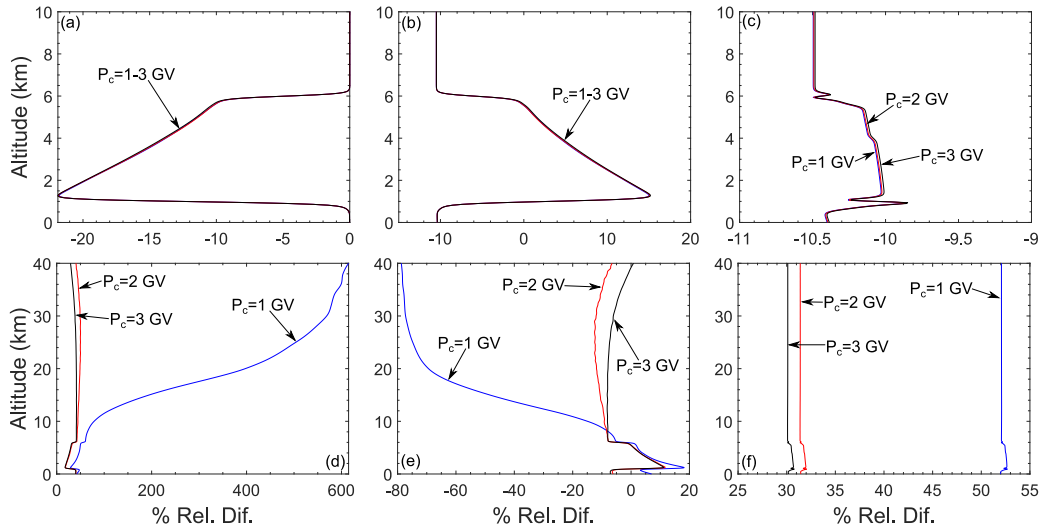
Fig. 10. Electrical properties of the fair weather atmosphere prior and at a timepoint equal to $t = 7000$ s (peak of GLE59 when occurs) in the presence of dust layer for locations with different cut-off rigidity value, P_c: **(a)** Percentage relative difference between the atmospheric conductivity in the presence of dust layer, and the fair weather conductivity in the absence of GLE59, **(b)** Percentage relative difference between the electric field magnitude in the presence of dust layer, and the fair weather value in the absence of GLE59, **(c)** Percentage relative difference between the current density magnitude in the presence of dust layer, and the fair weather value in the absence of GLE59, **(d)** percentage relative difference between conductivity at the peak of the event in the presence of dust layer and the ambient fair weather value prior to the event, **(e)** percentage relative difference between electric field magnitude at the peak of the event in the presence of dust layer and the ambient fair weather value prior to the event, **(f)** percentage relative difference between conduction current density magnitude at the peak of the event in the presence of dust layer and the ambient fair weather value prior to the event.

3.1.2. Atmospheric electrical properties in the presence of dust particles

In the presence of dust particles, ions attach to them, leading to depletion of ion number densities, and therefore, reducing the atmospheric electrical conductivity. Based on Eqs. (14)–(16), modification of the electrical conductivity results in modification of the electric field magnitude. Moreover, since the attachment coefficients depend on the ionic electrical mobility, which is different for positive and negative ions, the dust particles will acquire a net charge that, in general, is negative. However, it can also be positive if the dust particle number density is larger than the ion number density. Mallios et al. (2021b) provided an extensive study of the mechanism and its impact on the dust particle net charge, as well as on the modification of the ambient fair weather electrical conditions.

GLE59 case. Fig. 10a shows the conductivity reduction with respect to the fair weather value (percentage relative difference), caused by the ion attachment to dust particles, at different locations, and in the

absence of GLE event, at a time point equal to $t = 7000$ s (which corresponds to the peak of the GLE59 in the case it had happened). The percentage reduction is similar to all three locations since their fair weather conductivity distributions below 10 km are very similar (see Fig. 8a). The reduction decreases with respect to the latitude in the range of 1–6 km because the particle number density decreases with respect to the altitude due to the atmospheric scaling (Eq. (6) and Fig. 2b).

The system is almost at steady state, as the current density remains nearly constant regarding the altitude (Fig. 10c), and thus Eqs. (15) and (16) can be applied. The columnar resistance R_c increases in all cases by 11.4%, and since the conductivity at the ground is mainly unchanged, the electric field at the ground decreases according to the increase of the R_c, about 10%. As the conductivity decreases with respect to the fair weather value, it compensates for the increase of the columnar resistance and the electric field increases and vice versa (Fig. 10b). The
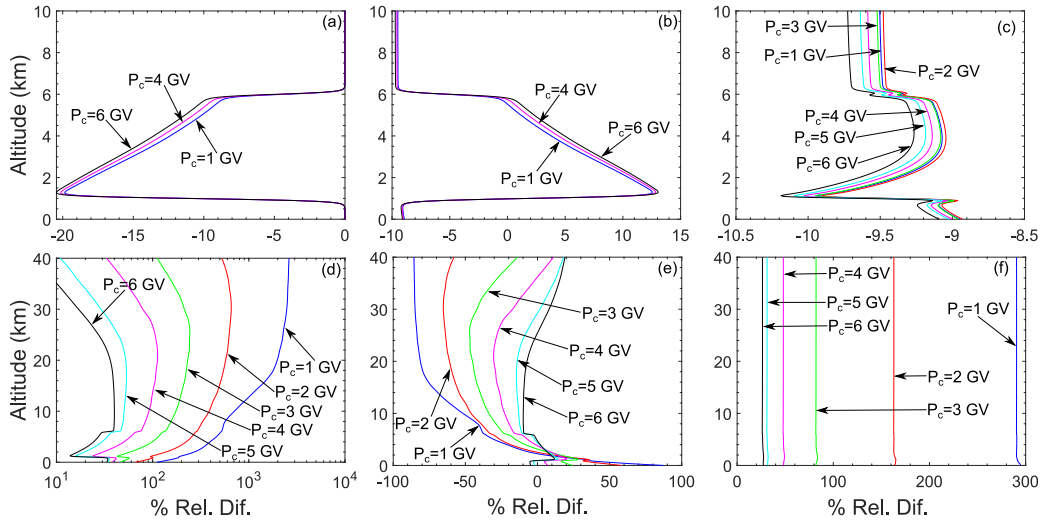
Fig. 11. The same as Fig. 10, but in the case of GLE05.

reduction of the current density magnitude occurs mainly due to the increase of the columnar resistance (Fig. 10c).

At the peak of GLE59, the enhancement of the ionization rate causes enhancement of the ion number density and influences the ion attachment process. Fig. 10d illustrates the modification of the conductivity at the peak of the event with respect to the fair weather value. Starting at the ground, the conductivity increases by 40% with respect to the fair weather value. As the altitude increases, the conductivity increase is rising. Inside the dust layer (1–6 km), the conductivity increase is falling due to the ion attachment process. Nevertheless, as opposed to the case where no GLE took place (Fig. 10a), inside the dust layer the conductivity was lower than the fair weather value. In the presence of the GLE, the conductivity is higher than the fair weather value. Finally, above the dust layer, the conductivity behavior is the same as in the case of GLE occurrence in fair weather conditions (Fig. 8d).

During GLE59, the columnar resistance decreases (since the conductivity increases). For $P_c = 3$ GV the decrease is 23% with respect to the fair weather value, for $P_c = 2$ GV it is 24%, and for $P_c = 1$ GV it is 34%. These decreases are very similar to the GLE59 occurrence in the absence of a dust layer. These reductions of the columnar resistance explain the enhancement of the current density magnitudes (Fig. 10f) and the vertical distribution of the electric field magnitude (Fig. 10b), following the logic presented in Section 3.1.1.

It can be concluded that the effects of the dust layer presence at the fair weather atmospheric electrical properties (conductivity reduction, columnar resistance increase, current density magnitude decrease) are canceled during GLE59. This happens due to the significant ion number density increase, which occurs because of the ionization rate amplification, which can compensate for the ion losses during the attachment process. It is emphasized that the ion attachment process is still present and still causes ion depletion, but since the ion number densities increase at values much larger than the fair weather values, the depletion is not sufficient to compensate for this increase. Therefore, the electrical conductivity and the current number density appear to increase during the event, as in the case of the dust layer absence.

GLE05 case. Similar analysis is performed in the case of GLE05 (Fig. 11). During this event, the cancellation of the dust layer effects at the fair weather atmospheric electrical properties is more apparent, and for regions with $P_c >= 2$ GV, this cancellation is total, and the results are the same as in the case of no dust layer (Fig. 9d–9f). As the cut-off rigidity values increases, the contribution of GLE05 vanishes, and the cancellation of the dust layer effects decreases. Nevertheless, even at $P_c = 6$ GV, there is a positive contribution and the atmospheric conductivity along with the current number density magnitude increase with respect to the fair weather value.

3.1.3. Dust particles electrical properties and dynamics

During the interaction of dust particles with the atmosphere, apart from modifying the atmospheric fair weather electrical properties, the electrical properties of dust particles are modified as well (Mallios et al., 2021b). In Section 3.1.2 the influence of the GLE events on the atmospheric electrical properties, as well on the modified atmospheric electrical properties in the presence of dust particles, was studied. In this Section, the influence of the GLE events on the electrical properties of dust particles is presented.

The electrical properties of the dust particles, such as the net charge or the electrical force that is acted upon them, or mechanical properties such as their settling velocity, are changing during their motion in the atmosphere (Mallios et al., 2021b). For the better representation of the results, we calculate the following average for a given quantity $f(t, z)$:

$$f_i = \frac{1}{t_{\text{end}}} \int_0^{t_{\text{end}}} \frac{\int_{z_{\text{min},i}}^{z_{\text{max},i}} f_i(t, z) N_{\text{p},i} dz}{\int_{z_{\text{min},i}}^{z_{\text{max},i}} N_{\text{p},i} dz} dt, \tag{17}$$

where the first integral over time is the temporal average throughout the GLE event, while the fraction inside the integral is the spatial weighted average based on the distribution of the particles of bin i along the altitude. The limits z_{min} and z_{max} are the spatial limiting points between which, $N_{\text{p},i} > 0$. The quantity f is the particle net charge, q_{p}, the electric field magnitude, E_z, the ratio between the electrical force and the gravity that act upon the particle, $RF = \frac{|F_{\text{el}}|}{|F_{\text{g}}|}$, and the particle terminal velocity, $|v|_{\text{p},\infty}$.

The ion attachment to dust particles process depends on the dust particle number density (Mallios et al., 2021b). Therefore, the discretization of the continuous particle size distribution presented by Ryder et al. (2013b) is of high importance for the correctness of the results. Mallios et al. (2021b) discretized the measured distribution using 19 bins, according to the following rule. 9 bins were chosen as bins of interest, between the size range 0.1 μm and 150 μm. These bins had a very narrow width, and their relative difference with the original distribution was less than 1%. The remaining bins, covering the rest of the sizes, were introduced for the accurate calculation of the cumulative effect of the entire particle size distribution to the ambient fair weather electrical properties. They showed that this methodology leads to an accurate calculation of the dust particles' electrical properties in the bins of interest, as well as the accurate modification of the large scale ambient electrical properties, such as the electric field, and the ion number densities. In the present work we follow this procedure, with the bins of interest being the bins $i = 1, 2, 4, 6, 8, 10, 12, 14, 16, 18$ (according to Table B.1). The averaged quantities are calculated for the selected bins of interest, and then using cubic interpolation (Press et al.,
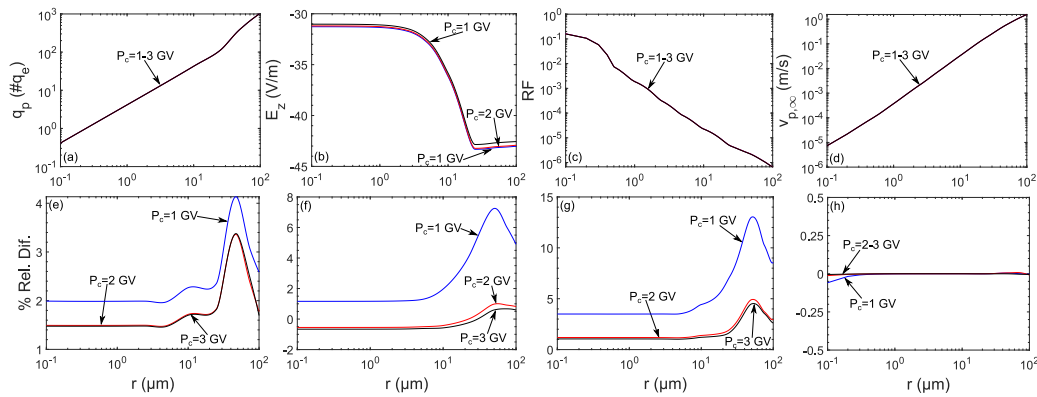
Fig. 12. Electrical properties of settling dust particles for different particle sizes, at locations with different cut-off rigidity value, P_c, with and without the GLE59, at time period equal to the duration of the GLE59: **(a)** Average particle net charge, in number of elementary charges, in the absence of GLE59, **(b)** average electric field magnitude "sensed" by particles during their settling, in the absence of GLE59, **(c)** average ratio between electric force magnitude and gravity, in the absence of GLE59, **(d)** average settling velocity, in the absence of GLE59, **(e)** percentage modification of the particle net charge during the occurrence of GLE59, **(f)** percentage modification of the electric field magnitude "sensed" by particles during the occurrence of GLE59, **(g)** percentage modification of the electric force magnitude over gravity ratio during the occurrence of GLE59, **(h)** percentage modification of the particle settling velocity during the occurrence of GLE59.

1992, p. 108), the corresponding values for the other sizes have been derived. We also note, that doubling the number of bins of interest (and consequently the number of total bins) modifies the generalization of the interpolation method by less than 0.6%.

GLE59 case. Fig. 12a illustrates the average net charge, given in a number of elementary charges, as a function of particle size, for locations with different P_c values, when the particles are left in the fair weather atmosphere and are let to fall for a period equal to the duration of the GLE event. All the sizes are negatively charged because the number densities are much smaller than the fair weather ion densities (Mallios et al., 2021b). Moreover, as the particle size increases, the particle net charge increases for two reasons. The first is that more ions can attach to particles as their sizes increase. The second is that large particles have small number densities, as can be seen by the measured mean normalized particle size distribution (Fig. 2a), and the available charge is divided among fewer particles, leading to a higher net charge per particle. This behavior is called particle competition, as described by Gunn (1954). The justification of the particle number density decrease as the particle size increases comes mainly from the fact that large particles settle quickly to the ground after their lift even in areas near the emission sources (Ryder et al., 2013a). Consequently to their settling process, large particles are observed at low altitudes (Ryder et al., 2013b), reducing their mean number density values in the altitude range of 1–6 km at which the measured size distribution is obtained.

Fig. 12b shows the average electric field that particles of each size "feel" as they move in the atmosphere for the given period. The negative sign means that the electric field points downwards. The electric field increases as the altitude decreases (Figs. 8b and 10b). The large particles settle faster than the small ones (Fig. 12d), and during the period under examination, they reach regions with a larger electric field magnitude than their small counterparts. This explains why the large particles, on average, are in a larger electric field than the small particles.

In Fig. 12c, the ratio between the electrical force magnitude and the magnitude of gravity is presented as a function of particle size. The electrical force is, in general, much smaller than gravity. For particles around 0.1 μm, the electrical force is one order of magnitude less than gravity, and in the case of giant particles ∼ 100 μm, the electrical force becomes 6 orders of magnitude less than gravity. The ratio between the forces increases as the size decreases because gravity (which is proportional to the cube of size) decreases faster than the electrical force (Mallios et al., 2021b). Moreover, given the negative charge polarity of the dust particle net charge, and the downwards pointing electric field, the electrical force points upwards in the opposite direction of

gravity. Nevertheless, given the small values of their ratio, the electrical force does not influence the terminal velocity of the dust particles.

The occurrence of GLE59 does not significantly alter the average electrical properties of the dust particles. The particle net charge increases between 1.5%–4% (Fig. 12e). The average electric field on the particles is nearly unaffected for locations with P_c = 2–3 GV, and it can reach a 7% increase for particles with r = 50 μm in regions with P_c = 1 GV (Fig. 12f). The ratio between the electric force magnitude and gravity, reaches a maximum 5% increase in regions with P_c = 2–3 GV, and a 13% increase in regions with P_c = 1 GV (Fig. 12g). All these effects are very small, leaving the settling velocity practically unaffected (Fig. 12h).

This behavior of the average quantities can be explained as follows. Based on the evolution of the GLE59 (Fig. 6a), it starts at t = 0 s (which is also the time point that the dust particles are introduced in the domain and are allowed to settle), it reaches its peak at t = 7000 s and then relaxes to the baseline value at t = 50000 s. Particles with sizes of up to 10 μm are in the domain for the whole duration of the event and experience its rise and fall. Therefore, the time average smooths any significant transient effect at the peak of the event. Particles with sizes between 10 μm and 50 μm, experience the rise of the event but have settled to the ground before the fall ends. Particles with sizes ∼ 50 μm experience the maximum contribution of the event. Finally, particles larger than 50 μm have settled before the event reaches its peak.

The contribution of the GLE event on the dust particle dynamics depends on the time dynamics both of the event and of the dust particles. The presented results quantify an expected range of contributions. The lower limit affects the small particles since they are present during the whole duration of the event. The maximum limit is the effect on particles with radius ∼ 50 μm because they experience the maximum contribution of the event.

GLE05 case. Similar reasoning applies in the case of GLE05 (Fig. 13). The electrical properties in the absence of the GLE event (Fig. 13a–13d) are very similar to the electrical properties of the previous case (Fig. 12a–12d). In the presence of the GLE05, the maximum contribution can reach 21% in terms of average charge, 32% in terms of average electric field magnitude, 70% in terms of average forces ratio, but still, these modifications are not sufficient to change the particle settling velocity (Figs. 13e–13h). The maximum distribution appears at particles ∼ 100 μm since in this case, the GLE05 has a very steep rising time and quite slow falling time (Fig. 6a), shifting the maximum contribution to larger particles (in smaller particles the contribution smooths out between the rise and fall periods).
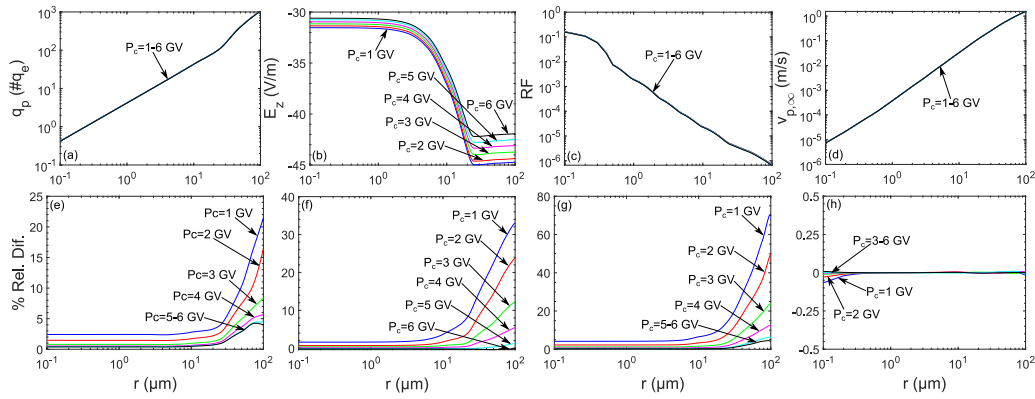
Fig. 13. The same as Fig. 12, but in the case of GLE05.
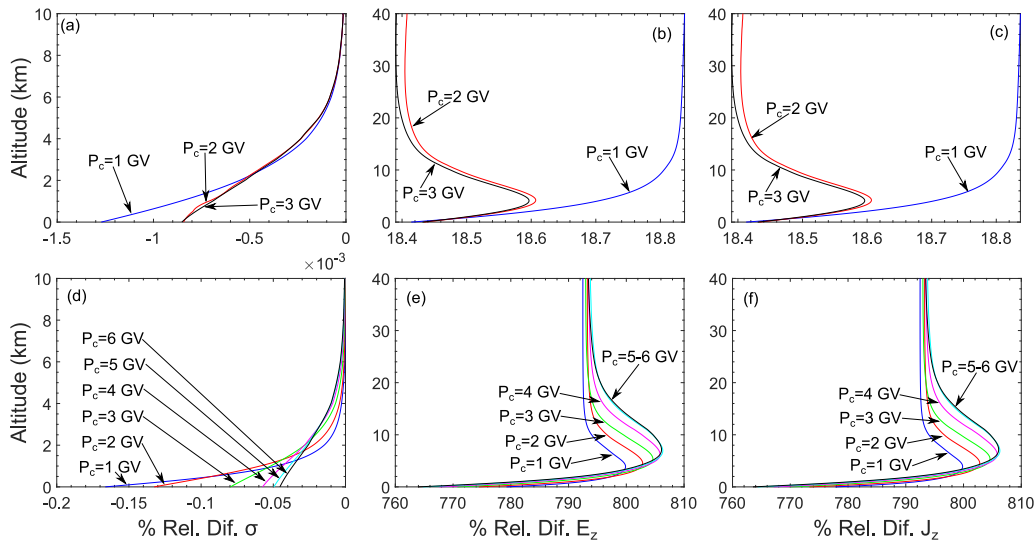
Fig. 14. Comparison between the cases of constant and variable IP in the fair weather electrical properties, at locations with different P_c values: **(a)** Percentage relative difference in conductivity vertical distributions for GLE59, **(b)** percentage relative difference in electric field magnitude vertical distributions for GLE59, **(c)** percentage relative difference in current density magnitude vertical distributions for GLE59, **(d)** percentage relative difference in conductivity vertical distributions for GLE5, **(e)** percentage relative difference in electric field magnitude vertical distributions for GLE5, **(f)** percentage relative difference in current density magnitude vertical distributions for GLE5.

3.2. Additional effects of the IP enhancement

In this case study, the IP is modified according to Eq. (13), consistently with observations and correlations presented by Markson (1981). All the comparisons presented in this Section are made with respect to the case of GLE occurrence but with constant IP.

3.2.1. Fair weather electrical properties
GLE59 case. Fig. 14a–c illustrates the percentage modification of the fair weather electrical properties, at locations with different cut-off rigidity values, if during the GLE59 there was an 18.6% increase of the IP (based on the discussion in Section 2.5). The increase in the potential is not significant, and no modification is observed in the atmospheric electrical conductivity (Fig. 14a).

In the absence of the ion attachment term, and for the given modification of the IP, Eq. (1) is in the linear region. This means that the electric field magnitude is modified in the range between 18.4–18.8%, similarly to the IP (Fig. 14b). The current density magnitude distribution follows the electric field magnitude distribution since the conductivity does not change (Fig. 14c).

GLE05 case. In the case of GLE05 the IP increases by 794.2% (based on the discussion in Section 2.5). The conductivity modification increases by two orders of magnitude, compared to the case of GLE59, but still is less than 1% and can be considered practically negligible (Fig. 14d).

For this increase in the potential, Eq. (1) is shifting towards the non-linear region, although they can still be considered. The electric field magnitude follows again the IP increase, but the modification range increases, and lies between 780%–805% (Fig. 14e). Similar behavior is observed in the current density magnitude (Fig. 14f).

3.2.2. Atmospheric electrical properties in the presence of dust particles
GLE59 case. Fig. 15a–c illustrates the percentage modification of the atmospheric electrical properties, at locations with different cut-off rigidity values, in the presence of settling dust particles, if during the GLE59 there was an 18.6% increase of the IP. The behavior of the system is similar to the fair weather case (Section 3.2.1). The conductivity modification is negligible (Fig. 15a), and the IP modification is reflected on the electric field magnitude (Fig. 15b), and the current density magnitude (Fig. 15c).

GLE05 case. Similar behavior is observed in the case of GLE05 (Fig. 15d–e).

3.2.3. Dust particles electrical properties and dynamics
GLE59 case. Increasing the IP by 18.6% has minimal effects on dust particles' electrical properties. The particle net charge is practically the same (Fig. 16a), but there is a slight increase between 4%–10% in the electric field "sensed" by the charged dust particles (Fig. 16b).
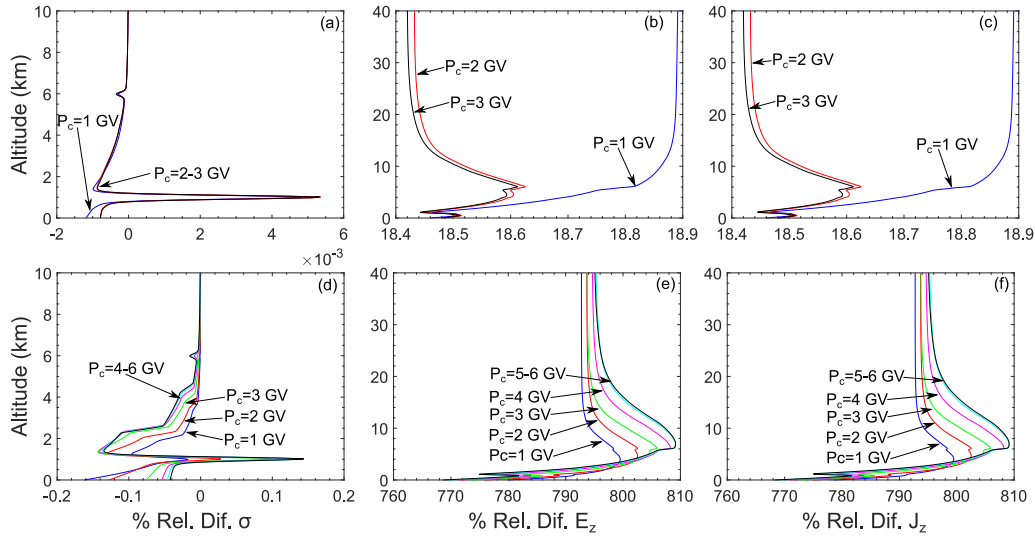
Fig. 15. Comparison between the cases of constant and variable IP in the modified atmospheric electrical properties in the presence of dust particles, at locations with different P_c values: **(a)** Percentage relative difference in conductivity vertical distributions for GLE59, **(b)** percentage relative difference in electric field magnitude vertical distributions for GLE59, **(c)** percentage relative difference in current density magnitude vertical distributions for GLE59, **(d)** percentage relative difference in conductivity vertical distributions for GLE5, **(e)** percentage relative difference in electric field magnitude vertical distributions for GLE5, **(f)** percentage relative difference in current density magnitude vertical distributions for GLE5.
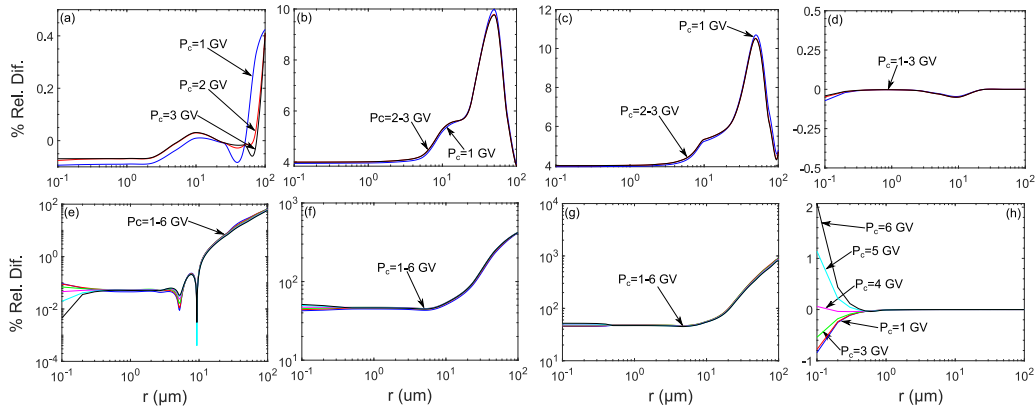
Fig. 16. Comparison between the cases of constant and variable IP in the electrical properties of settling dust particles, at locations with different P_c values: **(a)** Percentage relative difference in average charge for GLE59, **(b)** percentage relative difference in average electric field magnitude "sensed" by dust particles for GLE59, **(c)** percentage relative difference in electrical force magnitude over gravity ratio for GLE59, **(d)** percentage relative difference in particle terminal velocity for GLE59, **(e)** Percentage relative difference in average charge for GLE05, **(f)** percentage relative difference in average electric field magnitude "sensed' by dust particles for GLE05, **(g)** percentage relative difference in electrical force magnitude over gravity ratio for GLE05, **(h)** percentage relative difference in particle terminal velocity for GLE05.

Additionally, the electrical force magnitude over gravity ratio increases between 4%–11% (Fig. 16c). The maximum impact appears at particles with radius ∼ 50 μm since they experience the full impact of the event (as discussed in Section 3.1.3). Nevertheless, these modifications cannot alter dust particles dynamics in terms of terminal velocity (Fig. 16d).

GLE05 case. In the case of GLE05, with a possible increase of the IP by 794.2%, the electrical properties of the dust particles change significantly. The average net charge increases for particles with sizes in the range of 10–100 μm, while decreases for smaller particles in the range of 0.1–10 μm (Fig. 16e). The increase can reach up to 70% for particles ∼ 100 μm. On the other hand, the decrease can be considered practically negligible, and is less than 1% in the whole range.

The difference in the charging behavior can be attributed to the differences in the electric field "sensed" by the particles (Fig. 16f). For particles up to 10%, the increase of the electric field is ∼50%. This increase, along with the large number densities of the small particles, cannot significantly modify the behavior of the ion attachment process. On the other hand, for larger particles, this increase on the electric field can reach on average by 400%, and apparently is able to change the

ion attachment process by modifying the dominant mechanism between the diffusion and polarization process (Mallios et al., 2021b).

The electrical force magnitude over gravity ratio increases similarly to the electric field case (between 50%–800%, see Fig. 16g). Still, this increase is insufficient to alter the particle dynamic (Fig. 16h). It is noted that the small increase of the terminal velocity at small particles occurs because the percentage decrease of their net charge dominated over the percentage increase of the electric field.

4. Conclusions

We presented a consistent attempt to investigate the impact of GLE events on the atmospheric electric properties, and on dust particles charging mechanism through the ion attachment. Our results were consistent with observations and other models presented in the past literature. It has been found that in the case of fair weather conditions, GLE events enhance the atmospheric electrical conductivity, reduce the columnar resistance, and modify the fair weather electric field, air–earth conduction current, and possibly the Ionospheric Potential (IP) in a way that depends on the geomagnetic cut-off rigidity of

the location and the altitude. Specifically, as the cut-off rigidity of a location increases, then the GLE effects on the atmospheric electrical properties vanish. As the cut-off rigidity decreases, the air–earth conduction current magnitude increases. The electric field strength near the ground increases with the decreasing cut-off rigidity, and as the altitude increases the electric field strength decreases.

The terms of the IP, the modification is a bit more complicated. It is still unknown if the IP is modified directly by the GLEs and there is a lot of uncertainty in the understanding of the influence of solar activity on it. Under the assumption that there is a linear correlation between the measured count increase of NMs and the IP as presented by Markson (1981), then the IP can increase ∼20% in the case of GLE59, and ∼800% in the case of GLE05 with respect to the average GEC value of 205 kV. The air–earth conduction current magnitude and the electric field strength follow this increase of the IP.

On the other hand, under the assumption of unchanged IP, there is an increase of the air–earth conduction current, leading to an imbalance between to the charging and the discharging GEC currents. This means that either the IP should decrease for the equalization of these two currents, or that the imbalance is temporal due to the transient nature of the GLE effects, and ti will vanish when the GLE stops.

If a dust particle layer is present, GLE events tend to cancel its electrical effects in the ambient atmosphere. This means that the enhancement of the electric field and the reduction of atmospheric electrical conductivity, caused by the ion attachment to dust particles, not only tend to return to their ambient fair weather values, but they can be further modified as if the dust layer was not present as the event becomes more massive (as in the case of GLE05).

Finally, in terms of dust particles' electrical properties, GLE events tend to modify the ion attachment mechanism, and in principle, the particle net charge, and the electric field "sensed" by them increases. Nevertheless, since the electrical force magnitude is up to six orders of magnitude less than gravity, the increase of the particles' electrical properties are not sufficient to modify the particles settling dynamics and terminal velocities.

This study constitutes the first step towards a proper quantification of the solar activity-atmospheric electrical properties interaction. The following steps are towards modifying the presented 1D model to a time-dependent global model that can capture regional and global aspects of this interaction.

Declaration of competing interest

The authors declare that they have no known competing financial interests or personal relationships that could have appeared to influence the work reported in this paper.

Acknowledgments

Appendix A. List of physical constants

In Table A.1, the values of the physical constants used in the calculations throughout the paper are listed.

Appendix B. Particle size distribution binning

In Table B.1, the discrete bins of the size distribution are listed.

Table A.1
Physical constant values.

Symbol	Name	Value	Unit
R^*	Specific gas constant for dry air	287.058	J/(kg K)
k	Boltzmann constant	1.381×10^{-23}	m^{2}kg/(s^{2}K)
q_e	Elementary charge	1.602×10^{-19}	C
ε_0	Vacuum permittivity	8.854×10^{-12}	F/m
g	Gravitational acceleration	9.80665	m/s^2
ϱ_p	Mass density of dust particle	2600	kg/m^3

Table B.1
Discretization bins of the size distribution.

i	Bin$_i$ start (μm)	Bin$_i$ end (μm)	r_i (μm)	$N_{0,i}$ (m^{-3})
1	0.05	0.49754	0.11009	1.129286×10^8
2	0.49754	0.5025	0.5	7.29383×10^4
3	0.5025	0.9952	0.67089	2.088442×10^6
4	0.9952	1.005	1	2.196567×10^4
5	1.005	2.4877	1.4363	1.176378×10^6
6	2.4877	2.5125	2.5	4.171284×10^3
7	2.5125	4.976	3.4757	2.029122×10^5
8	4.976	5.025	5	2.045581×10^3
9	5.025	9.952	6.6764	8.080773×10^4
10	9.952	10.05	10	4.882423×10^2
11	10.05	24.878	13.132	1.42718×10^4
12	24.878	25.125	25	1.6105×10^1
13	25.125	49.756	30.175	3.065036×10^2
14	49.756	50.25	50	3.805×10^1
15	50.25	74.635	57.013	5.401142
16	74.635	75.375	75	2.673747×10^{-2}
17	75.375	99.514	83.132	3.160056×10^{-1}
18	99.514	100.5	100	3.303402×10^{-3}
19	100.5	150	112.55	3.96402×10^{-2}

Table C.1
Percentage increase with respect to the baseline during GLE59.

Neutron monitor station	Latitude (°)	Longitude (°)	% Increase
ALMA-ATA-B (AATB)	43.25	76.92	0[a]
APATITY (APTY)	67.55	33.33	33.47
CALGARY (CALG)	51.08	245.86	35.09
GOOSE BAY (GSBY)	53.27	299.6	35.1
HOBART (HBRT)	−42.9	147.33	18.3
HERMANUS (HRMS)	−34.42	19.22	0[a]
INUVIK (INVK)	68.35	226.28	26.91
IRKUTSK (IRKT)	52.47	104.03	2.6
JUNGFRAUJOCH (JUNG)	46.55	7.98	0[a]
KERGUELEN (KERG)	−49.35	70.22	28.37
KIEL (KIEL)	54.33	10.13	8.5
LOMNICKY (LMKS)	49.2	20.22	2.87
MCMURDO (MCMU)	−77.85	166.72	34.32
MAGADAN (MGDN)	60.12	151.02	12.78
MOSCOW (MOSC)	55.47	37.32	9.7
MT. WELLINGTON (MTWL)	−42.92	147.24	20.6
MAWSON (MWSN)	−67.6	62.88	34.45
MEXICO CITY (MXCO)	19.33	260.82	0[a]
NOVOSIBRSK (NVBK)	54.8	83	5.6
NEWARK (NWRK)	39.68	284.25	9.28
OULU (OULU)	65.05	25.47	29.27
POTCHEFSTROOM (PTFM)	−26.41	27.06	0[a]
ROME (ROME)	41.9	12.52	0[a]
SANAE (SNAE)	−70.3	357.65	39.39
SOUTH POLE (SOPO)	−90	0	57.93
TERRE ADELIE (TERA)	−66.65	140	26.94
THULE (THUL)	76.58	291.58	40.36
TSUMEB (TSMB)	−19.12	17.35	0[a]
TIXIE (TXBY)	71.6	128.9	24.82
YAKUTSK (YKTK)	62.02	129.7	16.75

[a]No de-trended NM data are available.

Appendix C. Neutron monitor measurements

In Tables C.1 and C.2, the percentage increase of each available NM count is listed, at the peak of GLE59 and GLE05, respectively.

Table C.2
Percentage increase with respect to the baseline during GLE05.

Neutron monitor station	Latitude (°)	Longitude (°)	% Increase
ALBUQUERQUE (ALBQ)	35.05	−106.62	1169.29
USSA ARNEB (ARNB)	−41.28	174.77	593.07
BERKELEY (BERK)	37.86	−123	987.5
CHICAGO (CHGO)	41.83	−87.7	2031.2
CLIMAX (CLMX)	39.37	−106.18	2704.57
GOTTINGEN (GOTT)	51.53	9.93	2619.28
HUANCAYO (HUAN)	−12.03	−75.33	36.9
LEEDS (LEED)	53.83	−1.58	5116.76
MT. NORIKURA (MTNR)	36.11	137.55	51.91
MT. WELLINGTON (MTWL)	−42.92	147.24	0[a]
MEXICO CITY (MXCO)	19.33	−99.18	123.09
OTTAWA (OTWA)	45.4	−75.6	2972.19
SACRAMENTO (SACR)	32.72	−105.75	987.5
STOCKHOLM (STHM)	59.35	17.95	4157.04
WEISSENAU (WEISS)	51	10	1956.4

[a]Although MTWL recorded GLE05, no de-trended NM data are available.

References

Asvestari, E., Willamo, T., Gil, A., Usoskin, I., Kovaltsov, G., Mikhailov, V., Mayorov, A., 2017. Analysis of ground level enhancements (GLE): Extreme solar energetic particle events have hard spectra. Adv. Space Res. 60 (4), 781–787.

Banjac, S., Herbst, K., Heber, B., 2019. The atmospheric radiation interaction simulator (AtRIS). J. Geophys. Res. Space Phys. 124, 50–67. http://dx.doi.org/10.1029/2018JA026042.

Barkley, A.E., Olson, N.E., Prospero, J.M., Gatineau, A., Panechou, K., Maynard, N.G., Blackwelder, P., China, S., Ault, A.P., Gaston, C.J., 2021. Atmospheric transport of North African dust-bearing supermicron freshwater diatoms to South America: Implications for iron transport to the equatorial North Atlantic ocean. Geophys. Res. Lett. 48 (5), http://dx.doi.org/10.1029/2020gl090476.

Baumgaertner, A.J.G., Lucas, G.M., Thayer, J.P., Mallios, S.A., 2014. On the role of clouds in the fair weather part of the global electric circuit. Atmos. Chem. Phys. 14 (16), 8599–8610. http://dx.doi.org/10.5194/acp-14-8599-2014.

Bazilevskaya, G., Usoskin, I., Flückiger, E., Harrison, R., Desorgher, L., Bütikofer, R., Krainev, M., Makhmutov, V., Stozhkov, Y.I., Svirzhevskaya, A., et al., 2008. Cosmic ray induced ion production in the atmosphere. Space Sci. Rev. 137 (1), 149–173.

Belov, A., Bieber, J., Eroshenko, E., Evenson, P., Gvozdevsky, B., Pchelkin, V., Pyle, R., Vashenyuk, V., Yanke, V., 2001. The "bastille day"; GLE 14 July, 2000 as observed by the worldwide neutron monitor network. In: International Cosmic Ray Conference, vol. 8, p. 3446.

Belov, A., Eroshenko, E., Mavromichalaki, H., Plainaki, C., Yanke, V., 2005. Solar cosmic rays during the extremely high ground level enhancement on 23 February 1956. Ann. Geophys. 23 (6), 2281–2291.

Bering, E.A., Few, A.A., Benbrook, J.R., 1998. The global electric circuit. Phys. Today 51 (10), 24–30. http://dx.doi.org/10.1063/1.882422.

Brooks, H.E., Lee, J.W., Craven, J.P., 2003. The spatial distribution of severe thunderstorm and tornado environments from global reanalysis data. Atmos. Res. 67–68, 73–94. http://dx.doi.org/10.1016/s0169-8095(03)00045-0.

Caballero-Lopez, R.A., Moraal, H., 2004. Limitations of the force field equation to describe cosmic ray modulation. J. Geophys. Res. Space Phys. 109, A01101. http://dx.doi.org/10.1029/2003JA010098.

Cliver, E.W., Hayakawa, H., Love, J.J., Neidig, D.F., 2020. On the size of the flare associated with the solar proton event in 774 AD. Astrophys. J. 903 (1), 41.

Cobb, W.E., 1967. Evidence of a solar influence on the atmospheric electric elements at Mauna Loa Observatory. Mon. Weather Rev. 95 (12), 905–911. http://dx.doi.org/10.1175/1520-0493(1967)095<0905:eoasio>2.3.co;2.

Cooke, D.J., 1983. Geomagnetic-cutoff distribution functions for use in estimating detector response to neutrinos of atmospheric origin. Phys. Rev. Lett. 51 (4), 320–323. http://dx.doi.org/10.1103/physrevlett.51.320.

van der Does, M., Knippertz, P., Zschenderlein, P., Giles Harrison, R., Stuut, J.-B.W., 2018. The mysterious long-range transport of giant mineral dust particles. Sci. Adv. 4 (12), http://dx.doi.org/10.1126/sciadv.aau2768.

Dorman, L.I., 2004. Cosmic Rays in the Earth's Atmosphere and Underground, vol. 303. Springer Science & Business Media.

Elhalel, G., Yair, Y., Nicoll, K., Price, C., Reuveni, Y., Harrison, R.G., 2014. Influence of short-term solar disturbances on the fair weather conduction current. J. Space Weather Space Clim. 4, A26. http://dx.doi.org/10.1051/swsc/2014022.

Ellison, M.A., 1957. Recent solar activity. Nature 180 (4596), 1173. http://dx.doi.org/10.1038/1801173a0.

Elsasser, W., Ney, E.P., Winckler, J.R., 1956. Cosmic-ray intensity and geomagnetism. Nature 178 (4544), 1226–1227. http://dx.doi.org/10.1038/1781226a0.

Farrell, W.M., Desch, M.D., 2002. Solar proton events and the fair weather electric field at ground. Geophys. Res. Lett. 29 (9), 37–1–37–4. http://dx.doi.org/10.1029/2001gl013908.

Fischer, H.J., Mühleisen, R., 1980. The ionospheric potential and the solar magnetic sector boundary crossings. Rep. Astron. Inst. D-7908, University of Tübingen, Ravensburg, Germany.

Gade, K., 2010. A non-singular horizontal position representation. J. Navig. 63 (3), 395–417. http://dx.doi.org/10.1017/s0373463309990415.

Gieseler, J., Heber, B., Herbst, K., 2017. An empirical modification of the force field approach to describe the modulation of galactic cosmic rays close to Earth in a broad range of rigidities. J. Geophys. Res. Space Phys. 122 (11), 10–964.

Gopalswamy, N., Xie, H., Akiyama, S., Yashiro, S., Usoskin, I., Davila, J., 2013. The first ground level enhancement event of solar cycle 24: Direct observation of shock formation and particle release heights. Astrophys. J. Lett. 765 (2), L30.

Gunn, R., 1954. Diffusion charging of atmospheric droplets by ions, and the resulting combination coefficients. J. Meteorol. 11 (5), 339–347. http://dx.doi.org/10.1175/1520-0469(1954)011<0339:DCOADB>2.0.CO;2.

Gunn, R., 1956. The hyperelectrification of raindrops by atmospheric electric fields. J. Meteorol. 13 (3), 283–288. http://dx.doi.org/10.1175/1520-0469(1956)013<0283:THORBA>2.0.CO;2.

Harrison, R.G., Nicoll, K.A., Mareev, E., Slyunyaev, N., Rycroft, M.J., 2020. Extensive layer clouds in the global electric circuit: Their effects on vertical charge distribution and storage. Proc. R. Soc. Lond. Ser. A Math. Phys. Eng. Sci. 476 (2238), http://dx.doi.org/10.1098/rspa.2019.0758.

Harrison, R.G., Nicoll, K.A., Ulanowski, Z., Mather, T.A., 2010. Self-charging of the Eyjafjallajökull volcanic ash plume. Environ. Res. Lett. 5 (2), http://dx.doi.org/10.1088/1748-9326/5/2/024004.

Harrison, R.G., Usoskin, I., 2010. Solar modulation in surface atmospheric electricity. J. Atmos. Sol.-Terr. Phys. 72 (2–3), 176–182. http://dx.doi.org/10.1016/j.jastp.2009.11.006.

Hays, P.B., Roble, R.G., 1979. A quasi-static model of global atmospheric electricity, 1. The lower atmosphere. J. Geophys. Res. 84 (A7), 3291. http://dx.doi.org/10.1029/ja084ia07p03291.

Herbst, K., Kopp, A., Heber, B., 2013. Influence of the terrestrial magnetic field geometry on the cutoff rigidity of cosmic ray particles. Ann. Geophys. 31, 1637–1643. http://dx.doi.org/10.5194/angeo-31-1637-2013.

Herbst, K., Kopp, A., Heber, B., Steinhilber, F., Fichtner, H., Scherer, K., Matthiä, D., 2010. On the importance of the local interstellar spectrum for the solar modulation parameter. J. Geophys. Res.: Atmos. 115 (D1), http://dx.doi.org/10.1029/2009JD012557.

Herbst, K., Muscheler, R., Heber, B., 2017. The new local interstellar spectra and their influence on the production rates of the cosmogenic radionuclides ^{10}Be and ^{14}C. J. Geophys. Res. Space Phys. 122, 23–34. http://dx.doi.org/10.1002/2016JA023207.

Holzworth, R., Mozer, F., 1979. Direct evidence of solar flare modification of stratospheric electric fields. J. Geophys. Res. 84 (C1), 363. http://dx.doi.org/10.1029/jc084ic01p00363.

Holzworth, R.H., Norville, K.W., Williamson, P.R., 1987. Solar flare perturbations in stratospheric current systems. Geophys. Res. Lett. 14 (8), 852–855. http://dx.doi.org/10.1029/gl014i008p00852.

Jánský, J., Pasko, V.P., 2015. Effects of conductivity perturbations in time-dependent global electric circuit model. J. Geophys. Res. 120 (12), http://dx.doi.org/10.1002/2015ja021604.

Kamra, A.K., 1972. Measurements of the electrical properties of dust storms. J. Geophys. Res. 77 (30), 5856–5869. http://dx.doi.org/10.1029/JC077i030p05856.

Kokorowski, M., Sample, J.G., Holzworth, R.H., Bering, E.A., Bale, S.D., Blake, J.B., Collier, A.B., Hughes, A.R.W., Lay, E., Lin, R.P., McCarthy, M.P., Millan, R.M., Moraal, H., O'Brien, T.P., Parks, G.K., Pulupa, M., Reddell, B.D., Smith, D.M., Stoker, P.H., Woodger, L., 2006. Rapid fluctuations of stratospheric electric field following a solar energetic particle event. Geophys. Res. Lett. 33 (20), http://dx.doi.org/10.1029/2006gl027718.

Landau, L.D., Lifshitz, E.M., 1963. Electrodynamics of Continuous Media, vol. 8. Pergamon Press.

Li, J.-G., 2008. Upstream nonoscillatory advection schemes. Mon. Weather Rev. 136 (12), 4709–4729. http://dx.doi.org/10.1175/2008MWR2451.1.

Mallios, S.A., Daskalopoulou, V., Amiridis, V., 2021a. Orientation of non spherical prolate dust particles moving vertically in the Earth's atmosphere. J. Aerosol Sci. 151, http://dx.doi.org/10.1016/j.jaerosci.2020.105657.

Mallios, S.A., Papangelis, G., Hloupis, G., Papaioannou, A., Daskalopoulou, V., Amiridis, V., 2021b. Modeling of spherical dust particle charging due to ion attachment. Front. Earth Sci. 9, http://dx.doi.org/10.3389/feart.2021.709890.

Markson, R., 1976. Ionospheric potential variations obtained from aircraft measurements of potential gradient. J. Geophys. Res. 81 (12), 1980–1990. http://dx.doi.org/10.1029/jc081i012p01980.

Markson, R., 1978. Solar modulation of atmospheric electrification and possible implications for the sun–weather relationship. Nature 273 (5658), 103–109. http://dx.doi.org/10.1038/273103a0.

Markson, R., 1981. Modulation of the Earth's electric field by cosmic radiation. Nature 291 (5813), 304–308. http://dx.doi.org/10.1038/291304a0.

Mironova, I.A., Aplin, K.L., Arnold, F., Bazilevskaya, G.A., Harrison, R.G., Krivolutsky, A.A., Nicoll, K.A., Rozanov, E.V., Turunen, E., Usoskin, I.G., 2015. Energetic particle influence on the Earth's atmosphere. Space Sci. Rev. 194 (1–4), 1–96. http://dx.doi.org/10.1007/s11214-015-0185-4.

Mishev, A., 2013. Short- and medium-term induced ionization in the Earth atmosphere by galactic and solar cosmic rays. Int. J. Atmos. Sci. 2013, http://dx.doi.org/10.1155/2013/184508.

Mishev, A.L., Kocharov, L.G., Usoskin, I.G., 2014. Analysis of the ground level enhancement on 17 May 2012 using data from the global neutron monitor network. J. Geophys. Res. Space Phys. 119 (2), 670–679.

Mishev, A.L., Velinov, P., 2014. Influence of hadron and atmospheric models on computation of cosmic ray ionization in the atmosphere—Extension to heavy nuclei. J. Atmos. Sol.-Terr. Phys. 120, 111–120.

Nicoll, K., Harrison, R., 2014. Detection of lower tropospheric responses to solar energetic particles at midlatitudes. Phys. Rev. Lett. 112 (22), http://dx.doi.org/10.1103/physrevlett.112.225001.

Nicoll, K.A., Harrison, R.G., Ulanowski, Z., 2010. Observations of Saharan dust layer electrification. Environ. Res. Lett. 6 (1), http://dx.doi.org/10.1088/1748-9326/6/1/014001.

NOAA/NASA/USAF, 1976. U.S Standard Atmosphere 1976. Technical Report NASA-TM-X-74335, NOAA-S/T-76-1562, Washington, DC, United States.

Đorđević, D., Tošić, I., Sakan, S., Petrović, S., Đuričić-Milanković, J., Finger, D.C., Dagsson-Waldhauserová, P., 2019. Can volcanic dust suspended from surface soil and deserts of Iceland Be transferred to central Balkan similarly to African dust (Sahara)? Front. Earth Sci. 7, http://dx.doi.org/10.3389/feart.2019.00142.

Papaioannou, A., Sandberg, I., Anastasiadis, A., Kouloumvakos, A., Georgoulis, M.K., Tziotziou, K., Tsiropoula, G., Jiggens, P., Hilgers, A., 2016. Solar flares, coronal mass ejections and solar energetic particle event characteristics. J. Space Weather Space Clim. 6, A42.

Papaioannou, A., Souvatzoglou, G., Paschalis, P., Gerontidou, M., Mavromichalaki, H., 2014. The first ground-level enhancement of solar cycle 24 on 17 May 2012 and its real-time detection. Sol. Phys. 289 (1), 423–436.

Pasko, V.P., Inan, U.S., Bell, T.F., Taranenko, Y.N., 1997. Sprites produced by quasi-electrostatic heating and ionization in the lower ionosphere. J. Geophys. Res. 102 (A3), 4529–4561. http://dx.doi.org/10.1029/96JA03528.

Poluianov, S.V., Usoskin, I.G., Mishev, A.L., Shea, M.A., Smart, D.F., 2017. GLE and sub-GLE redefinition in the light of high-altitude polar neutron monitors. Sol. Phys. 292 (11), 176. http://dx.doi.org/10.1007/s11207-017-1202-4, arXiv:1711.06161.

Press, W.H., Teukolsky, S.A., Vetterling, W.T., Flannery, B.P., 1992. Numerical Recipes in C: the Art of Scientific Computing, second Ed. Cambridge University Press, USA.

Raukunen, O., Vainio, R., Tylka, A.J., Dietrich, W.F., Jiggens, P., Heynderickx, D., Dierckxsens, M., Crosby, N., Ganse, U., Siipola, R., 2018. Two solar proton fluence models based on ground level enhancement observations. J. Space Weather Space Clim. 8, A04. http://dx.doi.org/10.1051/swsc/2017031.

Reiter, R., 1969. Solar flares and their impact on potential gradient and air-earth current characteristics at high mountain stations. Pure Appl. Geophys. 72 (1), 259–267. http://dx.doi.org/10.1007/bf00875709.

Renard, J.-B., Dulac, F., Durand, P., Bourgeois, Q., Denjean, C., Vignelles, D., Couté, B., Jeannot, M., Verdier, N., Mallet, M., 2018. In situ measurements of desert dust particles above the Western Mediterranean sea with the balloon-borne light optical aerosol counter/sizer (LOAC) during the ChArMEx campaign of summer 2013. Atmos. Chem. Phys. 18 (5), 3677–3699. http://dx.doi.org/10.5194/acp-18-3677-2018.

Roble, R.G., 1991. On modeling component processes in the Earth's global electric circuit. J. Atmos. Sol.-Terr. Phys 53 (9), 831–847. http://dx.doi.org/10.1016/0021-9169(91)90097-q.

Rycroft, M.J., Harrison, R.G., Nicoll, K.A., Mareev, E.A., 2008. An overview of Earth's global electric circuit and atmospheric conductivity. Space Sci. Rev 137, 83–105. http://dx.doi.org/10.1007/s11214-008-9368-6.

Rycroft, M.J., Israelsson, S., Price, C., 2000. The global atmospheric electric circuit, solar activity and climate change. J. Atmos. Sol.-Terr. Phys 62 (17), 1563–1576. http://dx.doi.org/10.1016/S1364-6826(00)00112-7.

Ryder, C.L., Highwood, E.J., Lai, T.M., Sodemann, H., Marsham, J.H., 2013a. Impact of atmospheric transport on the evolution of microphysical and optical properties of Saharan dust. Geophys. Res. Lett. 40 (10), 2433–2438. http://dx.doi.org/10.1002/grl.50482.

Ryder, C.L., Highwood, E.J., Rosenberg, P.D., Trembath, J., Brooke, J.K., Bart, M., Dean, A., Crosier, J., Dorsey, J., Brindley, H., Banks, J., Marsham, J.H., McQuaid, J.B., Sodemann, H., Washington, R., 2013b. Optical properties of Saharan dust aerosol and contribution from the coarse mode as measured during the Fennec 2011 aircraft campaign. Atmos. Chem. Phys. 13 (1), 303–325. http://dx.doi.org/10.5194/acp-13-303-2013.

Sartor, D., 1980. Electric field perturbations in terrestrial clouds and solar flare events. Mon. Weather Rev. 108 (4), 499–505. http://dx.doi.org/10.1175/1520-0493(1980)108<0499:efpitc>2.0.co;2.

Sheftel, V.M., Bandilet, O.I., Yaroshenko, A.N., Chernyshev, A.K., 1994. Space-time structure and reasons of global, regional, and local variations of atmospheric electricity. J. Geophys. Res. 99 (D5), 10797. http://dx.doi.org/10.1029/93jd02857.

Shepard, D., 1968. A two-dimensional interpolation function for irregularly-spaced data. In: Proceedings of the 1968 23rd ACM National Conference. ACM Press, http://dx.doi.org/10.1145/800186.810616.

Siingh, D., Gopalakrishnan, V., Singh, R.P., Kamra, A.K., Singh, S., Pant, V., Singh, R., Singh, A.K., 2007. The atmospheric global electric circuit: An overview. Atmos. Res. 84 (2), 91–110. http://dx.doi.org/10.1016/j.atmosres.2006.05.005.

Slyunyaev, N.N., Mareev, E.A., Zhidkov, A.A., 2015. On the variation of the ionospheric potential due to large-scale radioactivity enhancement and solar activity. J. Geophys. Res. 120 (8), 7060–7082. http://dx.doi.org/10.1002/2015ja021039.

Smart, D.F., Shea, M.A., 2005. A review of geomagnetic cutoff rigidities for earth-orbiting spacecraft. Adv. Space Res. 36 (10), 2012–2020. http://dx.doi.org/10.1016/j.asr.2004.09.015.

Souvatzoglou, G., Papaioannou, A., Mavromichalaki, H., Dimitroulakos, J., Sarlanis, C., 2014. Optimizing the real-time ground level enhancement alert system based on neutron monitor measurements: Introducing GLE alert plus. Space Weather 12 (11), 633–649.

Tacza, J., Raulin, J.-P., Mendonca, R.R.S., Makhmutov, V.S., Marun, A., Fernandez, G., 2018. Solar effects on the atmospheric electric field during 2010–2015 at low latitudes. J. Geophys. Res. 123 (21), 11,970–11,979. http://dx.doi.org/10.1029/2018JD029121.

Tegen, I., Hollrig, P., Chin, M., Fung, I., Jacob, D., Penner, J., 1997. Contribution of different aerosol species to the global aerosol extinction optical thickness: Estimates from model results. J. Geophys. Res. 102, 23895–23915. http://dx.doi.org/10.1029/97JD01864.

Tinsley, B.A., 2008. The global atmospheric electric circuit and its effects on cloud microphysics. Rep. Progr. Phys. 71 (6), 066801. http://dx.doi.org/10.1088/0034-4885/71/6/066801.

Tinsley, B.A., Zhou, L., 2006. Initial results of a global circuit model with variable stratospheric and tropospheric aerosols. J. Geophys. Res. 111 (D16), http://dx.doi.org/10.1029/2005JD006988.

Török, T., Downs, C., Linker, J.A., Lionello, R., Titov, V.S., Mikić, Z., Riley, P., Caplan, R.M., Wijaya, J., 2018. Sun-to-Earth MHD simulation of the 2000 July 14 "Bastille day" eruption. Astrophys. J. 856 (1), 75.

Toth III, J.R., Rajupet, S., Squire, H., Volbers, B., Zhou, J., Xie, L., Sankaran, R.M., Lacks, D.J., 2020. Electrostatic forces alter particle size distributions in atmospheric dust. Atmos. Chem. Phys. 20 (5), 3181–3190. http://dx.doi.org/10.5194/acp-20-3181-2020.

Tzur, I., Roble, R.G., 1985. The interaction of a dipolar thunderstorm with its global electrical environment. J. Geophys. Res. 90 (D4), 5989. http://dx.doi.org/10.1029/jd090id04p05989.

Ulanowski, Z., Bailey, J., Lucas, P.W., Hough, J.H., Hirst, E., 2007. Alignment of atmospheric mineral dust due to electric field. Atmos. Chem. Phys. 7 (24), 6161–6173. http://dx.doi.org/10.5194/acp-7-6161-2007.

Usoskin, I.G., Bazilevskaya, G.A., Kovaltsov, G.A., 2011. Solar modulation parameter for cosmic rays since 1936 reconstructed from ground-based neutron monitors and ionization chambers. J. Geophys. Res. 116 (A2), http://dx.doi.org/10.1029/2010ja016105.

Usoskin, I.G., Desorgher, L., Velinov, P., Storini, M., Flückiger, E.O., Bütikofer, R., Kovaltsov, G.A., 2009. Ionization of the Earth's atmosphere by solar and galactic cosmic rays. Acta Geophys. 57 (1), 88–101.

Usoskin, I., Koldobskiy, S., Kovaltsov, G., Gil, A., Usoskina, I., Willamo, T., Ibragimov, A., 2020a. Revised GLE database: Fluences of solar energetic particles as measured by the neutron-monitor network since 1956. Astron. Astrophys. 640, A17.

Usoskin, I.G., Koldobskiy, S.A., Kovaltsov, G.A., Rozanov, E.V., Sukhodolov, T.V., Mishev, A.L., Mironova, I.A., 2020b. Revisited reference solar proton event of 23 February 1956: Assessment of the cosmogenic-isotope method sensitivity to extreme solar events. J. Geophys. Res. 125 (6), http://dx.doi.org/10.1029/2020ja027921.

Usoskin, I.G., Kovaltsov, G.A., 2006. Cosmic ray induced ionization in the atmosphere: Full modeling and practical applications. J. Geophys. Res. 111 (D21), http://dx.doi.org/10.1029/2006jd007150.

Varga, G., Dagsson-Waldhauserová, P., Gresina, F., Helgadottir, A., 2021. Saharan dust and giant quartz particle transport towards Iceland. Sci. Rep. 11 (1), http://dx.doi.org/10.1038/s41598-021-91481-z.

Velinov, P.I., Asenovski, S., Kudela, K., Lastovicka, J., Mateev, L., Mishev, A., Tonev, P., 2013. Impact of cosmic rays and solar energetic particles on the Earth's ionosphere and atmosphere. J. Space Weather Space Clim. 3, A14.

Wedlund, C.S., Gronoff, G., Lilensten, J., Ménager, H., Barthélemy, M., 2011. Comprehensive calculation of the energy per ion pair or W values for five major planetary upper atmospheres. Ann. Geophys. 29 (1), 187–195. http://dx.doi.org/10.5194/angeo-29-187-2011.

Weinzierl, B., Ansmann, A., Prospero, J.M., Althausen, D., Benker, N., Chouza, F., Dollner, M., Farrell, D., Fomba, W.K., Freudenthaler, V., Gasteiger, J., Groß, S., Haarig, M., Heinold, B., Kandler, K., Kristensen, T.B., Mayol-Bracero, O.L., Müller, T., Reitebuch, O., Sauer, D., Schäfler, A., Schepanski, K., Spanu, A., Tegen, I., Toledano, C., Walser, A., 2017. The Saharan aerosol long-range transport and aerosol–cloud-interaction experiment: Overview and selected highlights. Bull. Am. Meteorol. Soc. 98 (7), 1427–1451. http://dx.doi.org/10.1175/BAMS-D-15-00142.1.

Willett, J.C., 1979. Solar modulation of the supply current for atmospheric electricity? J. Geophys. Res. 84 (C8), 4999. http://dx.doi.org/10.1029/jc084ic08p04999.

Yair, Y., Levin, Z., 1989. Charging of polydispersed aerosol particles by attachment of atmospheric ions. J. Geophys. Res. 94 (D11), 13085. http://dx.doi.org/10.1029/jd094id11p13085.

Zhou, L., Tinsley, B.A., 2007. Production of space charge at the boundaries of layer clouds. J. Geophys. Res. 112 (D11), http://dx.doi.org/10.1029/2006JD007998.

Zhou, L., Tinsley, B.A., 2012. Time dependent charging of layer clouds in the global electric circuit. Adv. Space Res. 50 (6), 828–842. http://dx.doi.org/10.1016/j.asr.2011.12.018.